공학박사학위논문

Compact finite difference methods using local analytic basis functions for the Helmholtz equation

헬름홀츠 방정식의 해석적 기저 함수를 이용한 컴팩트 유한 차분법

2017 년 8 월

서울대학교 대학원

기계항공공학부

박 현 서

Compact finite difference methods using local analytic basis functions for the Helmholtz equation

지도교수 이 건 우

이 논문을 공학박사 학위논문으로 제출함

2017 년 5 월

서울대학교 대학원

기계항공공학부

박 현 서

Hyunseo Park의 공학박사 학위논문을 인준함

2017 년 7 월

위 원 장	Changsoo Shin	(인)
부위원장	Kunwoo Lee	(인)
위 원	Dong-Joo Min	(인)
위 원	Churl-Hyun Jo	(인)
위 원	UGeun Jang	(인)

Abstract

Compact finite difference methods using local analytic basis functions for the Helmholtz equation are derived in this thesis. Compared to former compact finite difference methods, the proposed methods using the analytic information of the Helmholtz equation greatly reduce the numerical dispersion error so that the minimum number of grids per wavelength required in the numerical simulation can be lowered. This enables us to simulate the higher frequency/wavenumber range without increasing the number of grids, which reduces the computational costs. The proposed compact finite difference methods have great potential for numerically intensive applications using regular tensor product grids, because of their efficiency and accuracy. Some numerical results and comparisons are provided to verify the efficiency and accuracy of the proposed scheme. The proposed scheme is also applied to seismic wave propagation in heterogeneous media to assess its feasibility for geophysical applications.

Keywords: Helmholtz equation, Trefftz basis function, finite difference, numerical dispersion, seismic wave

Student Number: 2010-23217

Contents

Abstract **i**

Chapter 1 Introduction **1**

1.1 Background and Importance 1

1.2 Previous Works 2

1.3 Objectives 5

1.4 Organization of the Thesis 5

Chapter 2 Discretization using Analytic Basis Functions **7**

2.1 Preliminaries 7

2.1.1 Helmholtz Equation 7

2.1.2 Finite Difference Operator 8

2.1.3 Naïve Second Order Finite Difference Method 10

2.2 1D Compact Finite Difference Methods 11

2.2.1 3-Point Method 11

2.2.2 Alternative Derivation 12

2.3 2D Compact Finite Difference Methods 14

2.3.1 5-Point Method 16
2.3.2 9-Point Method 20
2.4 3D Compact Finite Difference Methods 23
2.4.1 7-Point Method 26
2.4.2 19-Point Method 26
2.4.3 27-Point Method 28
2.5 Source Amplitude Correction Functions 30
2.5.1 1D Source Amplitude Correction Function 30
2.5.2 2D Source Amplitude Correction Functions 33
2.5.3 3D Source Amplitude Correction Functions 39

Chapter 3 Dispersion Analysis and Numerical Experiments 44

3.1 Plane Wave Analysis 44
3.1.1 2D Dispersion Curves 44
3.1.2 3D Dispersion Curves 54
3.2 Numerical Solutions with the Impulse Source 62
3.2.1 2D 9-Point Method for a Homogeneous Medium 62
3.2.2 3D 27-Point Method for a Homogeneous Medium 72
3.2.3 2D Seismic Wave Propagation in Heterogeneous Media . . 82

Chapter 4 Conclusions 86

Appendix A Exact 1D Discretization with Piecewise-Constant Media 87

A.1 Derivation 87

Appendix B Perfectly Matched Layer **90**

B.1 Continuous Perfectly Matched Layer 90

B.2 Discrete Perfectly Matched Layer in 1D 91

B.3 Discrete Perfectly Matched Layer in 2D and 3D 92

Bibliography **94**

초록 **99**

List of Figures

Figure 2.1 1D stencil for a homogeneous medium 13

Figure 2.2 Neighbor nodal points centered at $u_{0,0}$ 17

Figure 2.3 Dispersion error curves for the naïve second order FDM and Nehrbass et al. (1998)'s second order FDM. Closer to zero is better. The vertical axis means the phase difference error when the wave propagates distance h. G is the number of grids per wavelength. 19

Figure 2.4 Three basic nodal summations in the 27-point compact stencil 25

Figure 2.5 The unnormalized sinc function 33

Figure 2.6 Source amplitude correction functions for the 2D impulse source. 38

Figure 2.7 The series approximation of $F_9(kh)$. The imaginary coefficients and log terms are omitted in the series approximation. 38

Figure 2.8 The source amplitude correction functions for the 3D impulse source. 42

Figure 2.9 The series expression of $F_{27}(kh)$. It matches well with $\mathrm{Re}(F_{27}(kh))$. 43

Figure 3.1 A schematic for describing the phase difference when the wave travels distance h with the propagation angle θ . . 45

Figure 3.2 Dispersion error curves for the 2D naïve second order method 50

Figure 3.3 Dispersion error curves for Nehrbass et al. (1998)'s 2D second order method 50

Figure 3.4 Dispersion error curves for Jo et al. (1996)'s method . . 51

Figure 3.5 Dispersion error curves for Singer and Turkel (1998)'s 2D fourth order method 51

Figure 3.6 Dispersion error curves for the 6th order method (Singer and Turkel, 2006; Sutmann, 2007; Nabavi et al., 2007) . 52

Figure 3.7 Dispersion error curves for Tsukerman (2006)'s method . 52

Figure 3.8 Dispersion error curves for the 9-point method of this thesis 53

Figure 3.9 The number of grids required to reach 1/8 cycle ($\pi/4$ radian) phase error for 2D methods. Higher is better. . . 53

Figure 3.10 Dispersion error curves for the 3D Naïve second order method 58

Figure 3.11 Dispersion error curves for Nehrbass et al. (1998)'s 3D second order method 58

Figure 3.12 Dispersion error curves for Operto et al. (2007)'s method based on Jo et al. (1996)'s approach 59

Figure 3.13 Dispersion error curves for the 19-point method of this thesis 59

Figure 3.14 Dispersion error curves for Sutmann (2007)'s method . . 60

Figure 3.15 Dispersion error curves for the 27-point method of this thesis 60

Figure 3.16 The number of grids to reach 1/8 cycle ($\pi/4$ radian) phase error for 3D methods. Higher is better. 61

Figure 3.17 Comparison between the analytic solution (solid line) and the discrete solution (dots) when $1/G = \tilde{k}h/2\pi = 0.01$. The discrete solution is obtained from the proposed 9-point method of this thesis with the single point approximation of the impulse source. 64

Figure 3.18 Comparison between the analytic solution (solid line) and the discrete solution (dots) when $1/G = \tilde{k}h/2\pi = 0.10$. The discrete solution is obtained from the proposed 9-point method of this thesis with the single point approximation of the impulse source. 65

Figure 3.19 Comparison between the analytic solution (solid line) and the discrete solution (dots) when $1/G = \tilde{k}h/2\pi = 0.20$. The discrete solution is obtained from the proposed 9-point method of this thesis with the single point approximation of the impulse source. 66

Figure 3.20 Comparison between the analytic solution (solid line) and the discrete solution (dots) when $1/G = \tilde{k}h/2\pi = 0.30$. The discrete solution is obtained from the proposed 9-point method of this thesis with the single point approximation of the impulse source. 67

Figure 3.21 Comparison between the analytic solution (solid line) and the discrete solution (dots) when $1/G = \tilde{k}h/2\pi = 0.30$. The discrete solution is obtained from the proposed 9-point method of this thesis with the 9-point approximation of the impulse source. 68

Figure 3.22 Comparison between the analytic solution (solid line) and the discrete solution (dots) when $1/G = \tilde{k}h/2\pi = 0.40$. The discrete solution is obtained from the proposed 9-point method of this thesis with the single point approximation of the impulse source. 69

Figure 3.23 Comparison between the analytic solution (solid line) and the discrete solution (dots) when $1/G = \tilde{k}h/2\pi = 0.40$. The discrete solution is obtained from the proposed 9-point method of this thesis with the 9-point approximation of the impulse source. 70

Figure 3.24 Pointwise L_1 error plot for $1/G = \tilde{k}h/2\pi = 0.30$. The solid line is computed from the single point approximation, and the dashed line is computed from the 9 point approximation of the impulse sources. 71

Figure 3.25 Pointwise L_1 error plot for $1/G = \tilde{k}h/2\pi = 0.40$. The solid line is computed from the single point approximation, and the dashed line is computed from the 9-point approximation of the impulse source. 71

Figure 3.26 Comparison between the analytic solution (solid line) and the discrete solution (dots) when $1/G = \tilde{k}h/2\pi = 0.01$. The discrete solution is obtained from the proposed 27-point method of this thesis with the single point approximation of the impulse source. 74

Figure 3.27 Comparison between the analytic solution (solid line) and the discrete solution (dots) when $1/G = \tilde{k}h/2\pi = 0.10$. The discrete solution is obtained from the proposed 27-point method of this thesis with the single point approximation of the impulse source. 75

Figure 3.28 Comparison between the analytic solution (solid line) and the discrete solution (dots) when $1/G = \tilde{k}h/2\pi = 0.20$. The discrete solution is obtained from the proposed 27-point method of this thesis with the single point approximation of the impulse source. 76

Figure 3.29 Comparison between the analytic solution (solid line) and the discrete solution (dots) when $1/G = \tilde{k}h/2\pi = 0.30$. The discrete solution is obtained from the proposed 27-point method of this thesis with the single point approximation of the impulse source. 77

Figure 3.30 Comparison between the analytic solution (solid line) and the discrete solution (dots) when $1/G = \tilde{k}h/2\pi = 0.30$. The discrete solution is obtained from the proposed 27-point method of this thesis with the 27-point approximation of the impulse source. 78

Figure 3.31 Comparison between the analytic solution (solid line) and the discrete solution (dots) when $1/G = \tilde{k}h/2\pi = 0.40$. The discrete solution is obtained from the proposed 27-point method of this thesis with the single point approximation of the impulse source. 79

Figure 3.32 Comparison between the analytic solution (solid line) and the discrete solution (dots) when $1/G = \tilde{k}h/2\pi = 0.40$. The discrete solution is obtained from the proposed 27-point method of this thesis with the 27-point approximation of the impulse source. 80

Figure 3.33 Pointwise L_1 error plot for $1/G = \tilde{k}h/2\pi = 0.30$. The solid line is computed from the single source approximation, and the dashed line is computed from the 27-point approximation. 81

Figure 3.34 Pointwise L_1 error plot for $1/G = \tilde{k}h/2\pi = 0.40$. The solid line is computed from the single source approximation, and the dashed line is computed from the 27-point approximation. 81

Figure 3.35 The Marmousi P-wave velocity model 84

Figure 3.36 Time domain seismograms from Tal-Ezer and the 9-point method 84

Figure 3.37 Comparison of time domain traces between Tal-Ezer's method and the 9-point method 85

Figure A.1 1D stencil for piecewise-constant heterogeneous media . 88

Chapter 1

Introduction

1.1 Background and Importance

The Helmholtz equation has been widely used in many applications including acoustics, elastic wave propagation and electromagnetics. Because the Helmholtz equation has an important role for such linear wave propagation, much research effort has been made to develop numerical methods for efficiently computing the solution of the Helmholtz equation. There are two main obstacles to efficiently solving the numerical solution of the Helmholtz equation. The first one is that the solution of the Helmholtz equation is highly oscillatory, which degrades the convergence rate of an iterative sparse matrix solver unless we employ a sophisticated preconditioner technique. Using a direct sparse matrix solver instead of an iterative solver, one might avoid the convergence rate problem from the oscillatory behavior, but the arithmetic and storage complexities become super-

linear with respect to degrees of freedom, which may hinder the applicability to large scale problems. There have been many published works to reduce the computational complexities of iterative and direct solvers by utilizing domain decomposition methods (see Gander and Zhang, 2016, and references therein) and $\mathcal{H}$-matrix techniques (e.g. Banjai and Hackbusch, 2007; Wang et al., 2011). The second obstacle is the dispersion error inherent in numerical methods. The dispersion error (or the phase error) comes when the trailing error terms are truncated in the discretization process. If the dispersion error is large, then a fine mesh is required to meet some desired level of accuracy, thus the computational costs increase. Therefore, reduction of the dispersion error is essential for large scale problems such as seismic wave propagation. In this thesis, we focus on reducing the dispersion error.

1.2 Previous Works

Several compact finite difference methods, which use only the direct neighbor nodal points locally on regular grids, have been proposed to reduce the numerical dispersion error, because the conventional second order finite difference method fails to give a reasonable accuracy unless the wavenumber or the frequency is quite low compared to the grid size. Although some higher order methods with extended finite difference stencils may also reduce the dispersion error, the compact stencil has some advantages such as easy implementation of boundary conditions and the reduced fill-in of sparse matrix factorization. There are some related works as follows:

Second order compact finite difference methods

Jo et al. (1996)'s work is popular in the exploration geophysics community. Jo et al. (1996)'s 9-point 2D compact stencil combines two different discretizations of the Laplacian operator and Marfurt (1984)'s idea, which mixes the consistent mass matrix and the lumped mass matrix derived from the finite element method. Jo et al. (1996) finds some weighting parameters to minimize a least squares objective function of the dispersion error. Although this method has second order of accuracy, the dispersion error is greatly reduced from the optimization. Jo et al. (1996)'s approach is extended to the 27-point 3D compact stencil by Operto et al. (2007).

Higher order compact finite difference methods

The conventional finite difference method gives second order of accuracy, whereas some higher order methods give 4th order and 6th order of accuracy without extending the length of the finite difference stencil. In 2D, the 4th order method (Singer and Turkel, 1998) and 6th order method (Singer and Turkel, 2006; Nabavi et al., 2007) use the 9-point compact stencil. In 3D, the 6th order method (Sutmann, 2007) uses the 27-point compact stencil. The central idea of the higher order methods is to transform the truncation error to computable terms by repeatedly applying the given partial differential equation to the truncation error, so that the computable terms are not errors anymore. The truncation error removal process continues until the desired order of accuracy is met.

Trefftz methods

Trefftz methods belong to a family of finite element methods that use trial and test functions that are locally exact solutions of the specific partial differential equation. The oscillatory basis functions of the Helmholtz equation can express the solution better than the conventional polynomial basis functions. The term *Trefftz basis function* can be used as a synonym for the term *analytic basis functions*. There are popular examples of Trefftz methods such as the method of fundamental solutions (MFS), the ultra weak variational formulation (UWVF) and the plane wave discontinuous Galerkin method (PWDG), etc. For detailed information about Trefftz methods for the Helmholtz equation, see Hiptmair et al. (2016), and references therein.

Compact finite difference methods using Trefftz basis functions

Trefftz basis functions well known in the finite element communities can be adopted to the compact finite difference methods. Nehrbass et al. (1998)'s 5-point stencil method in 2D and 7-point stencil method in 3D use the cylindrical and spherical Bessel functions as local analytic basis functions. Although the order of accuracy remains second order, the dispersion error of Nehrbass et al. (1998)'s method is better than that of the conventional second order method. A set of 2D plane waves is also used as local analytic basis functions on the 9-point stencil to simulate eletromagnetic wave propagation in Tsukerman (2006)'s work, which covers broad applications using local analytic basis functions in the finite difference framework. The plane wave basis functions also belong to Trefftz basis functions, which are able to significantly reduce the dispersion error.

All the methods listed above share the same principle in the sense that they use the analytic information of the Helmholtz equation. However, their dispersion characteristics might not be enough especially for large scale problems.

1.3 Objectives

In this thesis, we will focus on further reducing the numerical dispersion error in the context of compact finite difference methods by using local analytic basis functions which are called generalized harmonic polynomials (see Hiptmair et al., 2016) to squeeze out all the extra efficiency. We also derive source amplitude correction functions, which are required to match the amplitude of the discrete impulse response with that of the analytic impulse response in the improved range of the wavenumber/frequency due to the reduced dispersion error. After analyzing the dispersion characteristics of the proposed scheme, a seismic wave propagation problem is solved by the proposed scheme to examine its applicability to geophysical applications.

1.4 Organization of the Thesis

There are three remaining chapters in this thesis. Chapter 2 describes how to derive 1D, 2D and 3D compact finite difference methods incorporated with the analytic basis functions, and how to obtain source amplitude correction functions for the impulse source. In Chapter 3, the dispersion characteristics of some compact finite difference methods and the proposed methods are compared, and the accuracy of the numerical solutions with the source amplitude correction

functions is also verified. Then, the proposed scheme is applied to 2D seismic wave propagation. Finally, short conclusions for the proposed scheme are drawn in Chapter 4.

Chapter 2

Discretization using Analytic Basis Functions

We derive compact finite difference methods using local analytic basis functions. The analytic information of the Helmholtz equation can be exploited to greatly improve the accuracy and efficiency of the finite difference methods for the Helmholtz equation.

2.1 Preliminaries

2.1.1 Helmholtz Equation

For the computational domain $\Omega \subset \mathbb{R}^3$ and its boundary $\partial\Omega$, the boundary value problem (BVP) for the Helmholtz equation is expressed as

$$\begin{cases} -k^2 u - \nabla^2 u = f & \text{in } \Omega, \\ \text{some boundary conditions} & \text{on } \partial\Omega, \end{cases} \tag{2.1}$$

where k is the wavenumber, ∇^2 is the Laplacian operator and f is the source function. Appropriate boundary conditions such as free surface boundary conditions and the radiation boundary condition may be imposed. In this thesis, the scalar field u is assumed to be the pressure perturbation of the linear acoustics. Of course, u may represents other physical quantities such as the electromagnetic field.

Equation (2.1) can be expressed in Cartesian coordinates as

$$-k^2 u - \frac{\partial^2 u}{\partial x^2} - \frac{\partial^2 u}{\partial y^2} - \frac{\partial^2 u}{\partial z^2} = f, \tag{2.2}$$

which will be repeatedly used in this thesis.

The acoustic density ρ can be included as

$$-\frac{k^2}{\rho} u - \nabla \cdot \frac{1}{\rho} \nabla u = f, \tag{2.3}$$

and its Cartesian version is expressed as

$$-\frac{k^2}{\rho} u - \frac{\partial}{\partial x}\frac{1}{\rho}\frac{\partial u}{\partial x} - \frac{\partial}{\partial y}\frac{1}{\rho}\frac{\partial u}{\partial y} - \frac{\partial}{\partial z}\frac{1}{\rho}\frac{\partial u}{\partial z} = f. \tag{2.4}$$

2.1.2 Finite Difference Operator

We define a finite difference operator

$$\delta_x A(x) = \frac{A(x + h/2) - A(x - h/2)}{h}, \tag{2.5}$$

where h is the grid interval and $A(x)$ is an arbitrary function defined in some interval including $[-h/2, h/2]$. There is a connection between the finite difference operator δ_x and the differential operator $\partial_x := \frac{\partial}{\partial x}$. First, a shifting operator is

extracted from the Taylor series

$$\begin{aligned} B(x+h) &= \sum_{n=0}^{\infty} \frac{1}{n!}(h\partial_x)^n B(x) \\ &= \exp(h\partial_x)B(x), \end{aligned} \tag{2.6}$$

where B(x) is a smooth C^∞ differentiable function in some interval including $[0, h]$. The exponential expression $\exp(h\partial_x)$ is a pseudo differential operator that produces a translated function from the function $B(x)$ with a finite distance h. Using the pseudo differential operator, the finite difference operators in each coordinate direction can be expressed as

$$\begin{aligned} \delta_x &= \frac{1}{h}\left(\exp\left(\frac{h}{2}\partial_x\right) - \exp\left(-\frac{h}{2}\partial_x\right)\right) \\ &= \frac{2}{h}\sinh\left(\frac{h}{2}\partial_x\right), \\ \delta_y &= \frac{2}{h}\sinh\left(\frac{h}{2}\partial_y\right), \\ \delta_z &= \frac{2}{h}\sinh\left(\frac{h}{2}\partial_z\right), \end{aligned} \tag{2.7}$$

where $\sinh(z) = (\exp(z) - \exp(-z))/2$. As we can see, the finite difference operators are expressed as the hyperbolic function with the differential operators. δ_x can be expanded as

$$\begin{aligned} \delta_x &= \frac{2}{h}\sinh\left(\frac{h}{2}\partial_x\right) \\ &= \partial_x + \frac{h^2}{24}\partial_x^3 + \frac{h^4}{1920}\partial_x^5 + \frac{h^6}{322560}\partial_x^7 + \cdots, \end{aligned} \tag{2.8}$$

which has second order of accuracy. When $h \to 0$, the limits of δ_x, δ_y and δ_z approach to ∂_x, ∂_y and ∂_z, respectively.

We can also form second derivatives

$$\begin{aligned}\delta_x^2 &= \left(\frac{2}{h}\sinh\left(\frac{h}{2}\partial_x\right)\right)^2 \\ &= \frac{2\cosh(h\partial_x)-2}{h^2} \\ \delta_y^2 &= \frac{2\cosh(h\partial_y)-2}{h^2} \\ \delta_z^2 &= \frac{2\cosh(h\partial_z)-2}{h^2},\end{aligned} \tag{2.9}$$

which have the same effect with the conventional second order finite difference

$$\delta_x^2 F(x) = \frac{F(x+h)-2F(x)+F(x-h)}{h^2}. \tag{2.10}$$

2.1.3 Naïve Second Order Finite Difference Method

Using the finite difference operators of Equation (2.9), the spatial derivatives of the Helmholtz equation (Equation (2.2)) can be replaced by the discrete spatial derivatives as follows

$$-k^2u - \delta_x^2 u - \delta_y^2 u - \delta_z^2 u + O(h^2) = f. \tag{2.11}$$

Equation (2.11) does not perform well in the numerical simulation due to the severe truncation error. Ignoring the numerical error from discretization of the source function f, the second order truncation error $O(h^2)$ has an explicit series expression

$$\begin{aligned}&(\delta_x^2+\delta_y^2+\delta_z^2-\partial_x^2-\partial_y^2-\partial_z^2)u \\ &= \frac{h^2}{12}(\partial_x^4+\partial_y^4+\partial_z^4)u + \frac{h^4}{360}(\partial_x^6+\partial_y^6+\partial_z^6)u + \frac{h^6}{20160}(\partial_x^8+\partial_y^8+\partial_z^8)u + \dots,\end{aligned} \tag{2.12}$$

which is obtained from the series expansion of Equation (2.9). The truncation error can be significantly reduced by using some analytic knowledge of the underlying governing equation.

2.2 1D Compact Finite Difference Methods

2.2.1 3-Point Method

We start with the 1D Helmholtz equation with a homogeneous medium (a constant wavenumber k)

$$-k^2 u - \partial_x^2 u = 0, \tag{2.13}$$

where the source function f is omitted. The equation can be used to replace the spatial derivative $\partial_x^2 u$ with the scalar multiplication $-k^2 u$. Using this replacement, successive application of ∂_x^2 gives $(\partial_x^2)^n u = (-k^2)^n u$. The finite difference operator δ_x^2 can be manipulated as

$$\begin{aligned}
\delta_x^2 u &= \frac{2\cosh(h\partial_x) - 2}{h^2} u \\
&= \sum_{n=0}^{\infty} \frac{2}{(2n+2)!} h^{2n} (\partial_x^2)^{n+1} u \\
&= \sum_{n=0}^{\infty} \frac{2}{(2n+2)!} h^{2n} (-k^2)^{n+1} u \\
&= \frac{2\cos(kh) - 2}{h^2} u.
\end{aligned} \tag{2.14}$$

Note that the pseudo differential operator $\cosh(h\partial_x)$ is transformed to $\cos(kh)$. Rearranging Equation (2.14) gives

$$-\frac{2 - 2\cos(kh)}{h^2} u - \delta_x^2 u = 0, \tag{2.15}$$

which is a discrete analogue of the continuous version of the 1D Helmholtz equation (Equation (2.13)) without any discretization error. Using the function value $u_m = u(x_m)$ uniformly sampled at the discrete point x_m, we rewrite Equation (2.15) as

$$-\frac{2 - 2\cos(kh)}{h^2} u_m - \delta_x^2 u_m = 0, \tag{2.16}$$

or simply

$$-\frac{2-2\cos(kh)}{h^2}u_0 - \delta_x^2 u_0 = 0. \tag{2.17}$$

When the grid size h approaches to zero, Equation (2.15) approaches to the 1D Helmholtz equation (Equation (2.13)) as we can see the following limits

$$\begin{aligned} &\lim_{h\to 0}\frac{2-2\cos(kh)}{h^2} = k^2, \\ &\lim_{h\to 0}\delta_x^2 = \partial_x^2. \end{aligned} \tag{2.18}$$

2.2.2 Alternative Derivation

As we see in the previous section, any even function of the differential operator ∂_x can be transformed to the corresponding even function of the wavenumber k by using the Helmholtz equation (Equation (2.13)). By replacing ∂_x in even functions with ik, the 1D shifting operator (Equation (2.6)) can be manipulated as

$$\begin{aligned} \exp(h\partial_x) &= \cosh(h\partial_x) + \sinh(h\partial_x) \\ &= \cosh(h\partial_x) + \frac{\sinh(h\partial_x)}{h\partial_x}h\partial_x \\ &= \cosh(hik) + \frac{\sinh(hik)}{hik}h\partial_x \\ &= \cos(kh) + \operatorname{sinc}(kh)h\partial_x. \end{aligned} \tag{2.19}$$

Because $\sinh(x)$ is an odd function, the manipulation in the second line of Equation (2.19) is required to make the expression involving $\sinh(h\partial_x)$ even. The unnormalized sinc function is defined as

$$\operatorname{sinc}(x) = \frac{\sin(x)}{x}, \tag{2.20}$$

which will appear frequently in the rest of the thesis.

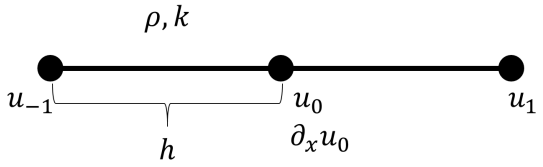

Figure 2.1: 1D stencil for a homogeneous medium

Using the 1D shifting operator, a nodal value that is separated by distance h can be written analytically as

$$\begin{aligned} u(h) &= \exp(h\partial_x)u_0 \\ &= (\cos(kh) + \operatorname{sinc}(kh)h\partial_x)u_0 \\ &= \cos(kh)u_0 + \operatorname{sinc}(kh)h\partial_x u_0 \end{aligned} \tag{2.21}$$

where u_0 is a nodal value of the solution at $x = 0$ and $\partial_x u_0$ is the first derivative at $x = 0$. Substituting $h \to \pm h$ into Equation (2.21) gives

$$u_1 := u(h) = \cos(kh)u_0 + \operatorname{sinc}(kh)h\partial_x u_0, \tag{2.22}$$

$$u_{-1} := u(-h) = \cos(kh)u_0 - \operatorname{sinc}(kh)h\partial_x u_0. \tag{2.23}$$

Summation of Equation (2.22) and (2.23) results in cancellation of the first derivative term and it gives a finite difference expression

$$u_{-1} + u_1 = 2\cos(kh)u_0, \tag{2.24}$$

which consists only of three local nodal points (Figure 2.1). Equation (2.24) can be solved by a tri-diagonal matrix system with proper boundary conditions. Equation (2.24) is equivalent to Equation (2.17) in the previous section. This derivation can be applied to obtain a finite difference method for 1D piecewise-constant heterogeneous media (Appendix A).

Note that Equation (2.21) can also be obtained from the general solution form

$$u(x) = A\cos(kx) + B\sin(kx), \tag{2.25}$$

where $A = u_0$ and $B = \frac{1}{k}\partial_x u_0$. $\cos(kx)$ and $\sin(kx)$ are the analytic basis functions of the 1D Helmholtz equation (Equation (2.13)).

2.3 2D Compact Finite Difference Methods

In this section, we develop compact finite difference methods for the 2D Helmholtz equation. Although we are tempted to extend the error-free approach of the 1D problems, there is no way to completely remove the truncation error in the 2D problem. Nevertheless, we try to maximally utilize the local analytic basis functions by combining neighbor nodal points as in the 1D problem.

A neighbor value of the 2D solution can be expressed in the polar coordinates (r, θ) by the 2D shifting operator as follows

$$u(r,\theta) = \exp(r\cos(\theta)\partial_x + r\sin(\theta)\partial_y)u_{0,0}, \tag{2.26}$$

where $u_{0,0}$ is a local reference nodal value at $r = 0$ to simplify the following derivation. To manipulate the 2D shifting operator, we can utilize the Jacobi-Anger expansion

$$\begin{aligned}\exp(iz\cos(\theta)) &= \sum_{n=-\infty}^{\infty} i^n J_n(z) e^{in\theta} \\ &= J_0(z) + 2\sum_{n=1}^{\infty} i^n J_n(z)\cos(n\theta),\end{aligned} \tag{2.27}$$

where $J_n(z)$ is the n-th order Bessel function of the first kind.

By using the Jacobi-Anger expansion, the 2D shifting operator can be expanded as

$$\begin{aligned}
&\exp(r\cos(\theta)\partial_x + r\sin(\theta)\partial_y) \\
=&\exp\left(ikr\left(\cos(\theta)\frac{\partial_x}{ik} + \sin(\theta)\frac{\partial_y}{ik}\right)\right) \\
=&\exp(ikr\cos(\theta-\psi)) \\
=&J_0(kr) + 2\sum_{n=1}^{\infty} i^n J_n(kr)\cos(n(\theta-\psi)) \\
=&J_0(kr) + 2\sum_{n=1}^{\infty} i^n J_n(kr)(\cos(n\theta)\cos(n\psi) + \sin(n\theta)\sin(n\psi)),
\end{aligned} \tag{2.28}$$

where $\cos\psi = \partial_x/ik$ and $\sin\psi = \partial_y/ik$. Also, the trigonometric identity $\cos(x-y) = \cos x\cos y + \sin x\sin y$ was used twice. We can check that

$$\begin{aligned}
\cos^2\psi + \sin^2\psi &= \left(\frac{\partial_x}{ik}\right)^2 + \left(\frac{\partial_y}{ik}\right)^2 \\
&= -\frac{1}{k^2}(\partial_x^2 + \partial_y^2) \\
&= 1
\end{aligned} \tag{2.29}$$

by using the operator relation $-k^2 - \partial_x^2 - \partial_y^2 = 0$ from the 2D Helmholtz equation without the source function f.

Plugging Equation (2.28) into Equation (2.26) gives

$$\begin{aligned}
u(r,\theta) &= J_0(kr)u_{0,0} + 2\sum_{n=1}^{\infty} i^n J_n(kr)(\cos(n\theta)\cos(n\psi) + \sin(n\theta)\sin(n\psi))u_{0,0} \\
&= J_0(kr)u_{0,0} + \sum_{n=1}^{\infty} J_n(kr)\left(A_n\cos(n\theta) + B_n\sin(n\theta)\right),
\end{aligned} \tag{2.30}$$

where $A_n = 2i^n\cos(n\psi)u_{0,0}$ and $B_n = 2i^n\sin(n\psi)u_{0,0}$. The Bessel functions with the trigonometric functions in the series are called generalized harmonic polynomials.

Note that seperation of variables in the polar coordinates (r, θ) gives the general solution of the 2D Helmholtz equation in the form of

$$u(r,\theta) = \sum_{n=0}^{\infty} (J_n(kr) + C_n Y_n(kr))(A_n \cos(n\theta) + B_n \sin(n\theta)), \tag{2.31}$$

where $Y_n(z)$ the n-th order Bessel function of the second kind, which has the logarithmic singularity at $z = 0$, whereas the 2D shifting operator version does not contain $Y_n(kr)$.

Equation (2.30) is a main building block to construct the finite difference methods in the following sections.

2.3.1 5-Point Method

The coefficients A_n and B_n in Equation (2.30) can be partly removed by using combination of neighbor nodal points. By setting $\theta \to \theta + \pi$ in Equation (2.30), the expansion of the analytic basis functions becomes

$$u(r,\theta+\pi) = J_0(kr)u_{0,0} + \sum_{n=1}^{\infty} J_n(kr)(-1)^n(A_n \cos(n\theta) + B_n \sin(n\theta)). \tag{2.32}$$

Because of the alternating sign $(-1)^n$ in the summation, we can eliminate some A_n and B_n when n is odd. Adding Equation (2.30) and Equation (2.32) gives

$$\begin{aligned} &u(r,\theta) + u(r,\theta+\pi) = \\ &\qquad 2J_0(kr)u_{0,0} + 2\sum_{n=1}^{\infty} J_{2n}(kr)(A_{2n} \cos(2n\theta) + B_{2n} \sin(2n\theta)). \end{aligned} \tag{2.33}$$

Similarly, we set $\theta \to \theta + \dfrac{\pi}{2}$ in Equation (2.33) to obtain

$$\begin{aligned} &u(r,\theta+\frac{\pi}{2}) + u(r,\theta+\frac{3\pi}{2}) = \\ &\qquad 2J_0(kr)u_{0,0} + 2\sum_{n=1}^{\infty} J_{2n}(kr)(-1)^n(A_{2n} \cos(2n\theta) + B_{2n} \sin(2n\theta)) \end{aligned} \tag{2.34}$$

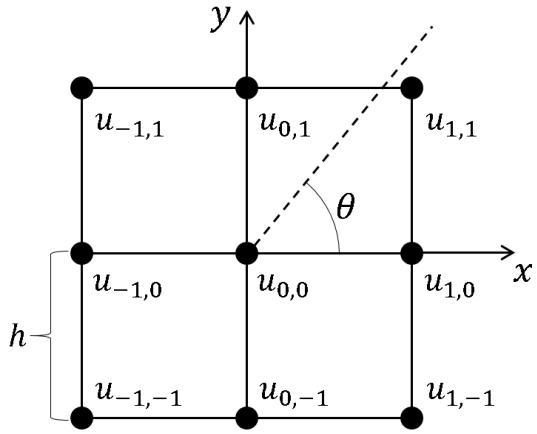

Figure 2.2: Neighbor nodal points centered at $u_{0,0}$

Adding Equation (2.33) and Equation (2.34) results in

$$u(r,\theta) + u(r,\theta+\frac{\pi}{2}) + u(r,\theta+\pi) + u(r,\theta+\frac{3\pi}{2}) = \\ 4J_0(kr)u_{0,0} + 4\sum_{n=1}^{\infty} J_{4n}(kr)(A_{4n}\cos(4n\theta) + B_{4n}\sin(4n\theta)). \tag{2.35}$$

Setting $r = h$ and $\theta = 0$, we rewrite the nodal values in the polar coordinates with subscripts that denote relative Cartesian coordinates to the reference node $u_{0,0}$ as shown in Figure 2.2. Then, we drop the summation part to form a 5-point stencil expression

$$u_{1,0} + u_{0,1} + u_{-1,0} + u_{0,-1} = 4J_0(kh)u_{0,0}, \tag{2.36}$$

which has second order of accuracy incurred from the truncation. Equation (2.36) can be cast into the finite difference form

$$-\frac{4 - 4J_0(kh)}{h^2}u_{0,0} - (\delta_x^2 + \delta_y^2)u_{0,0} = 0, \tag{2.37}$$

using the following relation

$$u_{1,0} + u_{0,1} + u_{-1,0} + u_{0,-1} = (h^2(\delta_x^2 + \delta_y^2) + 4)u_{0,0}. \tag{2.38}$$

The limit of the term containing the Bessel function approaches to k^2 as follows

$$\lim_{h \to 0} \frac{4 - 4J_0(kh)}{h^2} = k^2 \tag{2.39}$$

from the Taylor series expansion

$$4 - 4J_0(kh) = (kh)^2 - \frac{(kh)^4}{16} + \frac{(kh)^6}{576} - \frac{(kh)^8}{36864} + \dots . \tag{2.40}$$

The Bessel function need not be evaluated exactly. Evaluating the series up to 6th or 8th order gives nearly identical dispersion curves (Figure 2.3(b)) to those of the exact Bessel function in the kh interval $[0, \pi]$.

Note that Equation (2.36) is equivalent to Nehrbass et al. (1998)'s 5-point 2D finite difference method, which is better than the naïve finite difference method in terms of the numerical dispersion error. Figure 2.3(a) and Figure 2.3(b) show their dispersion characteristics. The phase error $(\tilde{k}h - kh)/2\pi$ should be close to zero along the horizontal axis $1/G$. More detailed explanation for the dispersion error will be given in Chapter 3.

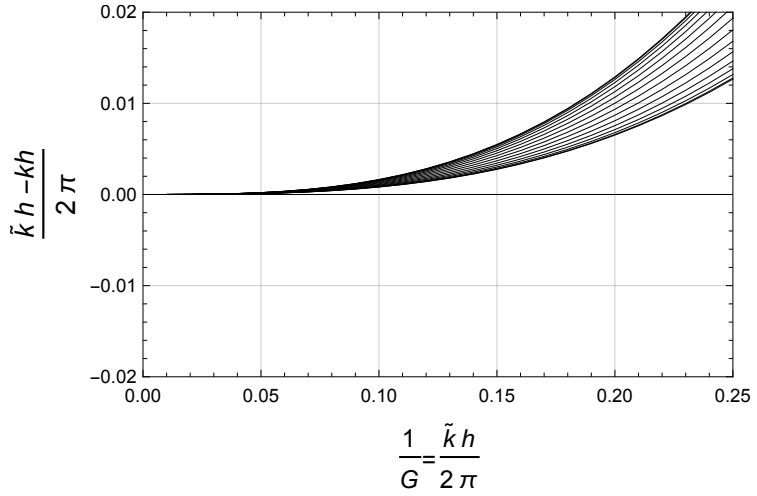

(a) Dispersion error curves for the naïve second order FDM.

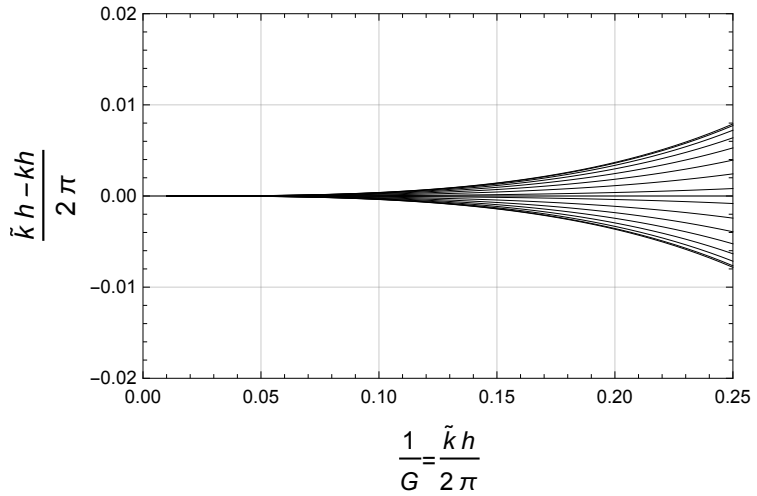

(b) Dispersion error curves for Nehrbass et al. (1998)'s second order FDM. The curves are closer to zero and more balanced than those of the naïve second order FDM.

Figure 2.3: Dispersion error curves for the naïve second order FDM and Nehrbass et al. (1998)'s second order FDM. Closer to zero is better. The vertical axis means the phase difference error when the wave propagates distance h. G is the number of grids per wavelength.

2.3.2 9-Point Method

We proceed to further remove the truncation error by employing more neighbor nodal points. Plugging $r \to \sqrt{2}r$ and $\theta \to \theta + \frac{\pi}{4}$ into Equation (2.35) gives

$$u(\sqrt{2}r,\theta + \frac{\pi}{4}) + u(\sqrt{2}r, \theta + \frac{3\pi}{4}) + u(\sqrt{2}r, \theta + \frac{5\pi}{4}) + u(\sqrt{2}r, \theta + \frac{7\pi}{4}) = 4J_0(\sqrt{2}kr)u_{0,0} + 4\sum_{n=1}^{\infty} J_{4n}(\sqrt{2}kr)(-1)^n(A_{4n}\cos(4n\theta) + B_{4n}\sin(4n\theta)). \tag{2.41}$$

Summation of Equation (2.35) and Equation (2.41) with the weight $1/J_4(kr)$ and $1/J_4(\sqrt{2}kr)$ gives

$$\frac{1}{J_4(kr)}\left(u(r,\theta) + u(r,\theta+\frac{\pi}{2}) + u(r,\theta+\pi) + u(r,\theta+\frac{3\pi}{2})\right) + \frac{1}{J_4(\sqrt{2}kr)}\left(u(\sqrt{2}r,\theta+\frac{\pi}{4}) + u(\sqrt{2}r,\theta+\frac{3\pi}{4}) + u(\sqrt{2}r,\theta+\frac{5\pi}{4}) + u(\sqrt{2}r,\theta+\frac{7\pi}{4})\right) = \left(\frac{4J_0(kr)}{J_4(kr)} + \frac{4J_0(\sqrt{2}kr)}{J_4(\sqrt{2}kr)}\right)u_{0,0} + 4\sum_{n=2}^{\infty}\left(\frac{J_{4n}(kr)}{J_4(kr)} + (-1)^n\frac{J_{4n}(\sqrt{2}kr)}{J_4(\sqrt{2}kr)}\right)(A_{4n}\cos(4n\theta) + B_{4n}\sin(4n\theta)), \tag{2.42}$$

where the summation begins from $n = 2$ because of the elimination when $n = 1$.

With $r = h$, $\theta = 0$, we truncate the summation part to obtain the following expression

$$\frac{1}{J_4(kh)}(u_{1,0} + u_{0,1} + u_{-1,0} + u_{0,-1}) + \frac{1}{J_4(\sqrt{2}kh)}(u_{1,1} + u_{-1,1} + u_{-1,-1} + u_{1,-1}) = \left(\frac{4J_0(kh)}{J_4(kh)} + \frac{4J_0(\sqrt{2}kh)}{J_4(\sqrt{2}kh)}\right)u_{0,0}. \tag{2.43}$$

Although Equation (2.43) can be implemented in its form as is, we further manipulate it by using the finite difference operators δ_x and δ_y to easily imple-

ment the Perfectly Matched Layer (PML) in the discrete level. The derivation of the discrete PML is shown in Appendix B. To include the finite difference operators, we use the following relations

$$\begin{aligned} u_{1,0} + u_{0,1} + u_{-1,0} + u_{0,-1} &= (h^2(\delta_x^2 + \delta_y^2) + 4)u_{0,0}, \\ u_{1,1} + u_{-1,1} + u_{-1,-1} + u_{1,-1} &= (2h^2(\delta_x^2 + \delta_y^2) + h^4\delta_x^2\delta_y^2 + 4)u_{0,0}. \end{aligned} \tag{2.44}$$

Inserting Equation (2.44) into Equation (2.43) and rearranging the resulting equation, we obtain the follwing finite difference expression

$$\begin{aligned} -\frac{1}{h^2}\left(\frac{4-4J_0(kh)}{J_4(kh)} + \frac{4-4J_0(\sqrt{2}kh)}{J_4(\sqrt{2}kh)}\right)u_{0,0} - \left(\frac{1}{J_4(kh)} + \frac{2}{J_4(\sqrt{2}kh)}\right)(\delta_x^2 + \delta_y^2)u_{0,0} \\ - \frac{1}{J_4(\sqrt{2}kh)}h^2\delta_x^2\delta_z^2 u_{0,0} = 0. \end{aligned} \tag{2.45}$$

By multiplying the inverse of the coefficient of $(\delta_x^2 + \delta_y^2)$, the final form is reorganized as

$$-\frac{L_9(kh)}{h^2}u_{0,0} - (\delta_x^2 + \delta_y^2)u_{0,0} - h^2 M_9(kh)\delta_x^2\delta_y^2 u_{0,0} = 0, \tag{2.46}$$

where

$$\begin{aligned} L_9(kh) &= \left(\frac{1}{J_4(kh)} + \frac{2}{J_4(\sqrt{2}kh)}\right)^{-1}\left(\frac{4-4J_0(kh)}{J_4(kh)} + \frac{4-4J_0(\sqrt{2}kh)}{J_4(\sqrt{2}kh)}\right), \\ M_9(kh) &= \left(\frac{J_4(\sqrt{2}kh)}{J_4(kh)} + 2\right)^{-1}. \end{aligned} \tag{2.47}$$

Directly evaluating the several Bessel functions would cause significant numerical overheads. $L_9(kh)$ and $M_9(kh)$ can be expressed as Taylor series

$$\begin{aligned} L_9(kh) &= (kh)^2 - \frac{(kh)^4}{12} + \frac{(kh)^6}{360} - \frac{13(kh)^8}{276480} + \frac{(kh)^{10}}{2073600} - \frac{13(kh)^{12}}{3715891200} + \dots, \\ M_9(kh) &= \frac{1}{6} + \frac{(kh)^2}{180} + \frac{(kh)^4}{8640} + \frac{(kh)^6}{518400} + \frac{(kh)^8}{464486400} + \dots. \end{aligned} \tag{2.48}$$

Although the truncation error of Equation (2.46) is $O(h^6)$, the minimum orders that should be evaluated for $L_9(kh)$ and $M_9(kh)$ are 10 and 6, respectively. Otherwise, the dispersion characteristic deteriorates. As in the 5-point case, the numerical error can get lowered by computing the higher order terms than 6th order even if the equation has $O(h^6)$ error. $L_9(kh)$ and $M_9(kh)$ can be efficiently evaluated by the Horner's rule (Horner, 1819). Note that one might use the Chebyshev polynomial $T_n(x)$ with the Clenshaw's three term recurrence formula (Clenshaw, 1955) to approximate $L_9(kh)$ and $M_9(kh)$ for minimizing maximal pointwise error (the minimax property of the Chebyshev polynomial), although there would be nonvanishing error when $kh \to 0$, if the order of the Chebyshev polynomials is not high enough.

Some 6th order methods (Singer and Turkel, 2006; Sutmann, 2007; Nabavi et al., 2007) give the truncated series

$$\begin{aligned} L_{6\text{th}}(kh) &= (kh)^2 - \frac{(kh)^4}{12} + \frac{(kh)^6}{360}, \\ M_{6\text{th}}(kh) &= \frac{1}{6} + \frac{(kh)^2}{180}, \end{aligned} \tag{2.49}$$

which are equivalent to the low order terms in Equation (2.48). The dispersion characteristic of the 6th order method will be compared with our method later in Chapter 3.

We may slightly modify Equation (2.46) to

$$-\frac{L_9(kh)}{h^2} u_{0,0} - (\delta_x^2 + \delta_y^2) u_{0,0} - h^2 \delta_x \delta_y M_9(kh) \delta_x \delta_y u_{0,0} = 0, \tag{2.50}$$

which would be helpful for efficient numerical implementation due to symmetry of the resulting discretization when the equation is applied to heterogeneous

media and the PML (Appendix B), although the 9-point method was derived on the homogeneity assumption.

2.4 3D Compact Finite Difference Methods

The solution of the 3D Helmholtz equation can be expanded with the analytic basis functions as follows

$$\begin{aligned} u(r,\theta,\phi) &= \sum_{l=0}^{\infty}\sum_{m=-l}^{l} C_{lm} j_l(kr) Y_l^m(\theta,\phi) \\ &= \sum_{l=0}^{\infty}\sum_{m=-l}^{l} C_{lm} j_l(kr) \sqrt{\frac{(l-m)!}{(l+m)!}} P_l^m(\cos\theta) e^{im\phi}, \end{aligned} \tag{2.51}$$

where $j_l(z)$ is the l-th order spherical Bessel function of the first kind, $Y_l^m(\theta,\phi)$ is the spherical harmonic function, and $P_l^m(z)$ is the associated Legendre function. The polar angle θ and the azimuthal angle ϕ in the spherical coordinates are restricted to the intervals $[0,\pi]$ and $[0,2\pi)$, respectively. Also, C_{lm} is an unknown coefficient to be eliminated by the combination of the neighbor nodal points to obtain higher-order expressions as we conducted in the 2D cases. The analytic function expression can be derived by applying the plane wave expansion of the spherical wave to the 3D shifting operator as the Jacobi-Anger expansion is used in the 2D case. Or simply, we can use the general solution without the spherical Bessel function of the second kind $y_l(kr)$.

Because the derivation of the 3D finite difference methods is somewhat lengthy, so we suggest three basic building blocks to ease the derivation of the 3D finite difference methods as follows:

6-Point Summation

This is a summation of the six nodes with distance h from the reference node $u_{0,0,0}$ at $r = 0$. The participating nodes are displayed in Figure 2.4(a).

$$\begin{aligned} & u_{1,0,0} + u_{-1,0,0} + u_{0,1,0} + u_{0,-1,0} + u_{0,0,1} + u_{0,0,-1} \\ &= 6j_0(kh)u_{0,0,0} + j_4(kh)\left(\frac{7}{2}C_{40} + \frac{1}{2}\sqrt{\frac{35}{2}}(C_{4,-4} + C_{44})\right) \\ &\quad + j_6(kh)\left(\frac{3}{4}C_{60} - \frac{3}{4}\sqrt{\frac{7}{2}}(C_{6,-4} + C_{64})\right) + O(h^8). \end{aligned} \tag{2.52}$$

12-Point Summation

This is a summation of the twelve nodes whose distance is $\sqrt{2}h$ from the center node $u_{0,0,0}$. The participating nodes are displayed in Figure 2.4(b).

$$\begin{aligned} & u_{1,1,0} + u_{-1,-1,0} + u_{1,-1,0} + u_{-1,1,0} \\ & + u_{0,1,1} + u_{0,-1,-1} + u_{0,1,-1} + u_{0,-1,1} \\ & + u_{1,0,1} + u_{-1,0,-1} + u_{-1,0,1} + u_{1,0,-1} \\ &= 12j_0(\sqrt{2}kh)u_{0,0,0} + j_4(\sqrt{2}kh)\left(-\frac{7}{4}C_{40} - \frac{1}{4}\sqrt{\frac{35}{2}}(C_{4,-4} + C_{44})\right) \\ &\quad + j_6(\sqrt{2}kh)\left(-\frac{39}{16}C_{60} + \frac{39}{16}\sqrt{\frac{7}{2}}(C_{6,-4} + C_{64})\right) + O(h^8) \end{aligned} \tag{2.53}$$

8-Point Summation

This is a summation of the eight nodes whose distance is $\sqrt{3}h$ from the

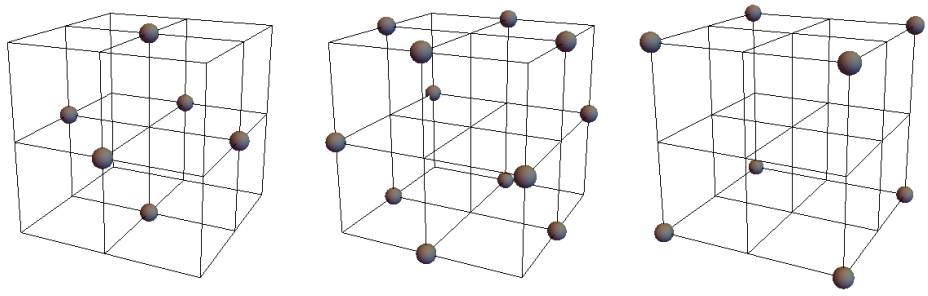

(a) 6-point (b) 12-point (c) 8-point

Figure 2.4: Three basic nodal summations in the 27-point compact stencil

center node $u_{0,0,0}$. The participating nodes are displayed in Figure 2.4(c).

$$\begin{aligned} & u_{1,1,1} + u_{-1,-1,-1} + u_{1,1,-1} + u_{-1,-1,1} \\ & + u_{1,-1,1} + u_{-1,1,-1} + u_{1,-1,-1} + u_{-1,1,1} \\ & = 8j_0(\sqrt{3}kh)u_{0,0,0} + j_4(\sqrt{3}kh)\left(-\frac{28}{9}C_{40} - \frac{2}{9}\sqrt{70}(C_{4,-4} + C_{44})\right) \\ & \qquad + j_6(\sqrt{3}kh)\left(\frac{16}{9}C_{60} - \frac{8}{9}\sqrt{14}(C_{6,-4} + C_{64})\right) + O(h^8) \end{aligned} \tag{2.54}$$

By combining the three building blocks, we derive several compact finite difference methods in the following sections.

2.4.1 7-Point Method

If we use only the 6-point summation, it gives the 7-point stencil (including the center node $u_{0,0,0}$) method equivalent to Nehrbass et al. (1998)'s work. Using the following relation

$$\begin{aligned} & u_{1,0,0} + u_{-1,0,0} + u_{0,1,0} + u_{0,-1,0} + u_{0,0,1} + u_{0,0,-1} \\ & = (h^2(\delta_x^2 + \delta_y^2 + \delta_z^2) + 6)u_{0,0,0}, \end{aligned} \tag{2.55}$$

Equation (2.52) can be expressed as a finite difference form

$$-\frac{6 - 6j_0(kh)}{h^2}u_{0,0,0} - (\delta_x^2 + \delta_y^2 + \delta_z^2)u_{0,0,0} = 0, \tag{2.56}$$

which has second order of accuracy. Its numerical dispersion characteristic is better than the naïve second order finite difference method (Equation (2.11)), although the accuracy is not enough in the range of high wavenumber k. The function $(6 - 6j_0(kh))$ has the following series expansion

$$6 - 6j_0(kh) = (kh)^2 - \frac{(kh)^4}{20} + \frac{(kh)^6}{840} - \frac{(kh)^8}{60480} + \dots . \tag{2.57}$$

2.4.2 19-Point Method

By combining the 6-point and 12-point summations with appropriate weighting, a 4th order method using the 19-point stencil can be obtained as follows

$$\begin{aligned} & A_{19}(kh)(u_{1,0,0} + u_{-1,0,0} + u_{0,1,0} + u_{0,-1,0} + u_{0,0,1} + u_{0,0,-1}) \\ & + B_{19}(kh)(u_{1,1,0} + u_{-1,-1,0} + u_{1,-1,0} + u_{-1,1,0} \\ & \quad + u_{0,1,1} + u_{0,-1,-1} + u_{0,1,-1} + u_{0,-1,1} \\ & \quad + u_{1,0,1} + u_{-1,0,-1} + u_{-1,0,1} + u_{1,0,-1}) \\ & \quad = D_{19}(kh)u_{0,0,0}, \end{aligned} \tag{2.58}$$

where

$$\begin{aligned} A_{19}(kh) &= j_4(\sqrt{2}kh) \\ B_{19}(kh) &= 2j_4(kh) \\ D_{19}(kh) &= 6j_0(kh)A_{19}(kh) + 12j_0(\sqrt{2}kh)B_{19}(kh). \end{aligned} \tag{2.59}$$

Using Equation (2.55) and the following relation

$$\begin{aligned} &u_{1,1,0} + u_{-1,-1,0} + u_{1,-1,0} + u_{-1,1,0} \\ &+ u_{0,1,1} + u_{0,-1,-1} + u_{0,1,-1} + u_{0,-1,1} \\ &+ u_{1,0,1} + u_{-1,0,-1} + u_{-1,0,1} + u_{1,0,-1} \\ &= (4h^2(\delta_x^2 + \delta_y^2 + \delta_z^2) + h^4(\delta_x^2\delta_y^2 + \delta_y^2\delta_z^2 + \delta_z^2\delta_x^2) + 12)u_{0,0,0}, \end{aligned} \tag{2.60}$$

Equation (2.58) becomes

$$-\frac{L_{19}(kh)}{h^2}u_{0,0,0} - (\delta_x^2 + \delta_y^2 + \delta_z^2)u_{0,0,0} - h^2 M_{19}(kh)(\delta_x^2\delta_y^2 + \delta_y^2\delta_z^2 + \delta_z^2\delta_x^2)u_{0,0,0} = 0, \tag{2.61}$$

where

$$\begin{aligned} L_{19}(kh) &= \frac{6A_{19}(kh) + 12B_{19}(kh) - D_{19}(kh)}{A_{19}(kh) + 4B_{19}(kh)}, \\ M_{19}(kh) &= \frac{B_{19}(kh)}{A_{19}(kh) + 4B_{19}(kh)}. \end{aligned} \tag{2.62}$$

As in the 2D 9-point case, $L_{19}(kh)$ and $M_{19}(kh)$ are approximated by the Taylor series expansions

$$\begin{aligned} L_{19}(kh) &= (kh)^2 - \frac{(kh)^4}{12} + \frac{17(kh)^6}{5544} - \frac{3373(kh)^8}{57081024} + \frac{8447(kh)^{10}}{13454812800} + \cdots, \\ M_{19}(kh) &= \frac{1}{6} + \frac{(kh)^2}{396} + \frac{5(kh)^4}{679536} - \frac{43(kh)^6}{224246880} + \cdots. \end{aligned} \tag{2.63}$$

2.4.3 27-Point Method

We employ all the three summations to eliminate all the coefficients (C_{40}, C_{60}, $C_{4,-4}$, C_{44}, $C_{6,-4}$ and C_{64}) as follows

$$\begin{aligned}
&A_{27}(kh)(u_{1,0,0}+u_{-1,0,0}+u_{0,1,0}+u_{0,-1,0}+u_{0,0,1}+u_{0,0,-1})\\
+&B_{27}(kh)(u_{1,1,0}+u_{-1,-1,0}+u_{1,-1,0}+u_{-1,1,0}\\
&\quad +u_{0,1,1}+u_{0,-1,-1}+u_{0,1,-1}+u_{0,-1,1}\\
&\quad +u_{1,0,1}+u_{-1,0,-1}+u_{-1,0,1}+u_{1,0,-1})\\
+&C_{27}(kh)(u_{1,1,1}+u_{-1,-1,-1}+u_{1,1,-1}+u_{-1,-1,1}\\
&\quad +u_{1,-1,1}+u_{-1,1,-1}+u_{1,-1,-1}+u_{-1,1,1})\\
&\quad =D_{27}(kh)u_{0,0,0},
\end{aligned} \tag{2.64}$$

where

$$\begin{aligned}
A_{27}(kh) &= 312j_4(\sqrt{3}kh)j_6(\sqrt{2}kh)+128j_4(\sqrt{2}kh)j_6(\sqrt{3}kh)\\
B_{27}(kh) &= 96j_4(\sqrt{3}kh)j_6(kh)+256j_4(kh)j_6(\sqrt{3}kh)\\
C_{27}(kh) &= 351j_4(kh)j_6(\sqrt{2}kh)-54j_4(\sqrt{2}kh)j_6(kh)\\
D_{27}(kh) &= 6j_0(kh)A_{27}(kh)+12j_0(\sqrt{2}kh)B_{27}(kh)+8j_0(\sqrt{3}kh)C_{27}(kh).
\end{aligned} \tag{2.65}$$

The weighting function $C_{27}(kh)$ is irrelavent to the coefficient C_{lm}. Using Equation (2.55) and Equation (2.60) and the following relation

$$\begin{aligned}
&u_{1,1,1}+u_{-1,-1,-1}+u_{1,1,-1}+u_{-1,-1,1}\\
+&u_{1,-1,1}+u_{-1,1,-1}+u_{1,-1,-1}+u_{-1,1,1}\\
&=(4h^2(\delta_x^2+\delta_y^2+\delta_z^2)+2h^4(\delta_x^2\delta_y^2+\delta_y^2\delta_z^2+\delta_z^2\delta_x^2)+h^6\delta_x^2\delta_y^2\delta_z^2+8)u_{0,0,0},
\end{aligned} \tag{2.66}$$

Equation (2.64) becomes the 27-point finite difference expression

$$-\frac{L_{27}(kh)}{h^2}u_{0,0,0} - (\delta_x^2+\delta_y^2+\delta_z^2)u_{0,0,0} - h^2 M_{27}(kh)(\delta_x^2\delta_y^2+\delta_y^2\delta_z^2+\delta_z^2\delta_x^2)u_{0,0,0} \\ -h^4 N_{27}(kh)\delta_x^2\delta_y^2\delta_z^2 u_{0,0,0} = 0, \tag{2.67}$$

where

$$\begin{aligned} L_{27}(kh) &= \frac{6A_{27}(kh)+12B_{27}(kh)+8C_{27}(kh)-D_{27}(kh)}{A_{27}(kh)+4B_{27}(kh)+4C_{27}(kh)} \\ M_{27}(kh) &= \frac{B_{27}(kh)+2C_{27}(kh)}{A_{27}(kh)+4B_{27}(kh)+4C_{27}(kh)} \\ N_{27}(kh) &= \frac{C_{27}(kh)}{A_{27}(kh)+4B_{27}(kh)+4C_{27}(kh)}. \end{aligned} \tag{2.68}$$

Equation (2.67) can be slightly modified to

$$-\frac{L_{27}(kh)}{h^2}u_{0,0,0} - (\delta_x^2+\delta_y^2+\delta_z^2)u_{0,0,0} - h^2\delta_x\delta_y M_{27}(kh)\delta_x\delta_y u_{0,0,0} \\ -h^2\delta_y\delta_z M_{27}(kh)\delta_y\delta_z u_{0,0,0} \\ -h^2\delta_z\delta_x M_{27}(kh)\delta_z\delta_x u_{0,0,0} \\ -h^4\delta_x\delta_y\delta_z N_{27}(kh)\delta_x\delta_y\delta_z u_{0,0,0} = 0, \tag{2.69}$$

which can be used to include the discrete Perfectly Matched Layer symmetrically (Appendix B) and mild heterogeneity, although the order of accuracy decreases to first order due to the interface error.

The Taylor series of $L_{27}(kh)$, $M_{27}(kh)$ and $N_{27}(kh)$ are given as

$$\begin{aligned} L_{27}(kh) &= (kh)^2 - \frac{(kh)^4}{12} + \frac{(kh)^6}{360} - \frac{(kh)^8}{22464} + \frac{1273(kh)^{10}}{3150576000} - \frac{5749(kh)^{12}}{1867661452800} + \cdots, \\ M_{27}(kh) &= \frac{1}{6} + \frac{(kh)^2}{180} + \frac{(kh)^4}{9360} + \frac{11(kh)^6}{7956000} + \frac{4021(kh)^8}{424468512000} + \cdots, \\ N_{27}(kh) &= \frac{1}{30} + \frac{(kh)^2}{540} + \frac{127(kh)^4}{2237625} + \frac{158(kh)^6}{127544625} + \frac{39360019(kh)^8}{1894190734800000} + \cdots. \end{aligned} \tag{2.70}$$

The low order terms of these series match with the series of Sutmann (2007)'s 6th order method as follows

$$\begin{aligned} L_{6\text{th}}(kh) &= (kh)^2 - \frac{(kh)^4}{12} + \frac{(kh)^6}{360}, \\ M_{6\text{th}}(kh) &= \frac{1}{6} + \frac{(kh)^2}{180}, \\ N_{6\text{th}}(kh) &= \frac{1}{30}. \end{aligned} \tag{2.71}$$

2.5 Source Amplitude Correction Functions

The amplitude mismatch between the discrete and analytic solutions for the impulse source is quite significant especially when a naïve implementation of the impulse source is used in the extended wavenumber range, thus correction for the amplitude mismatch must be considered. We only deal with the impulse source in this thesis. For smoothly distributed sources, see 6th order compact finite difference methods (Singer and Turkel, 2006; Sutmann, 2007; Nabavi et al., 2007).

2.5.1 1D Source Amplitude Correction Function

In Section 2.2.1, we determined the 1D discrete Helmholtz operator (Equation (2.15)) without the source function f. To consider a set of impulse sources (the Dirac delta distribution) in the discrete framework, we manipulate the

continuous Helmholtz equation with the discrete Helmholtz operator as follows

$$\begin{aligned}
(-k^2 - \partial_x^2)u &= f \\
u &= (-k^2 - \partial_x^2)^{-1} f \\
u_m &= [(-k^2 - \partial_x^2)^{-1} f]_m \\
\left(-\frac{2-2\cos(kh)}{h^2} - \delta_x^2\right) u_m &= \left(-\frac{2-2\cos(kh)}{h^2} - \delta_x^2\right) [(-k^2 - \partial_x^2)^{-1} f]_m,
\end{aligned} \tag{2.72}$$

where the subscript m means a discrete sampling operation from a continuous function (e.g. $u_m = u(x_m)$).

Equation (2.72) is a formal expression that requires an exact solution $(-k^2 - \partial_x^2)^{-1} f$. Fortunately in the 1D problem, a discrete source function that generates the exact solution for series of the Dirac delta functions $f(x) = \sum_l \alpha_l \delta(x - x_l)$ exists. α_l is a strength for the Dirac delta function at $x = x_l$. We assume that the source location x_l is exactly on the discrete sampled nodes, although impulse sources at arbitrary locations (e.g. between two sampled nodes) are not difficult to consider.

If the imaginary part of k is positive ($\mathrm{Im}\, k > 0$), the analytic solution for the series of impulse sources is expressed as

$$(-k^2 - \partial_x^2)^{-1} f = \sum_l \frac{i}{2k} \exp(ik|x - x_l|)\alpha_l, \tag{2.73}$$

which is a weighted summation of Green's functions (impulse responses) for the 1D Helmholtz equation. Then, the right hand side of the fourth line of

Equation (2.72) becomes

$$\begin{aligned}
&\left(-\frac{2-2\cos(kh)}{h^2}-\delta_x^2\right)[(-k^2-\partial_x^2)^{-1}f]_m \\
&=\left(-\frac{2-2\cos(kh)}{h^2}-\delta_x^2\right)\sum_l \frac{i}{2k}\exp(ik|x_m-x_l|)\alpha_l \\
&=\sum_l \mathrm{sinc}(kh)\frac{\alpha_l}{h}\delta_{lm} \\
&=\mathrm{sinc}(kh)\frac{\alpha_m}{h},
\end{aligned} \tag{2.74}$$

where δ_{lm} is the Kronecker delta function defined as

$$\delta_{lm}=\begin{cases}0 & \text{if } l\neq m,\\ 1 & \text{if } l=m.\end{cases} \tag{2.75}$$

Using Equation (2.74), Equation (2.72) becomes

$$-\frac{2-2\cos(kh)}{h^2}u_m-\delta_x^2 u_m=\mathrm{sinc}(kh)\frac{\alpha_m}{h}, \tag{2.76}$$

which is able to produce the exact solution from the series of impulse sources. We set $m=0$ for simplicity as follows

$$-\frac{2-2\cos(kh)}{h^2}u_0-\delta_x^2 u_0=\mathrm{sinc}(kh)\frac{\alpha_0}{h}. \tag{2.77}$$

The $\mathrm{sinc}(kh)$ function may be thought of as a correction term for the finite volume approximation of the Dirac delta function

$$\frac{\alpha_0}{h}=\frac{\displaystyle\int_{x_0-\frac{h}{2}}^{x_0+\frac{h}{2}}\alpha_0\delta(x-x_0)\,\mathrm{d}x}{\displaystyle\int_{x_0-\frac{h}{2}}^{x_0+\frac{h}{2}}\mathrm{d}x}, \tag{2.78}$$

which is an average of the source term within a grid cell whose size is h. Figure 2.5 shows the $\mathrm{sinc}(kh)$ function. If we conduct a 1D simulation with

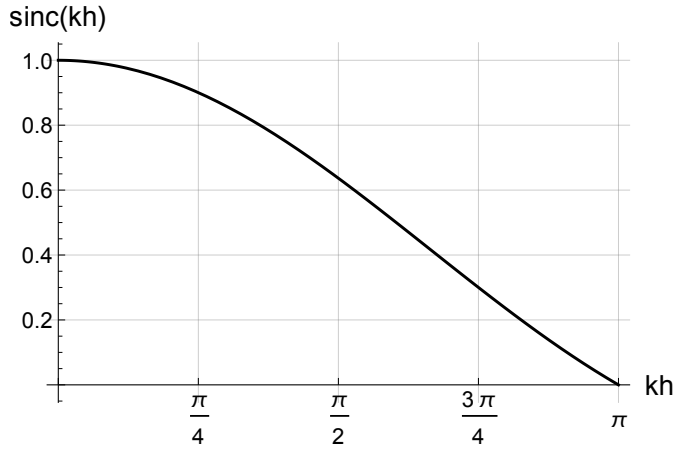

Figure 2.5: The unnormalized sinc function

$kh = \pi/2$ (the number of grids per wavelength $G = 2\pi/kh = 4$), then the sinc function has the value about 0.637. If we use only the naïve finite volume approximation of the source term (Equation (2.78)) without $\mathrm{sinc}(kh)$, the amplitude of the numerical solution would have $1/0.637 = 1.57$ times as large as the amplitude of the analytic solution.

2.5.2 2D Source Amplitude Correction Functions

The source amplitude correction is essential also for 2D. As we derived the source amplitude correction term $\mathrm{sinc}(kh)$ for the 1D problem in Section 2.5.1, we apply the discrete Helmholtz operator to the analytic solution with the source f as follows

$$\left(-\frac{L_9(kh)}{h^2} - (\delta_x^2 + \delta_y^2) - h^2 M_9(kh)\delta_x^2\delta_y^2\right) u_{0,0} = \left(-\frac{L_9(kh)}{h^2} - (\delta_x^2 + \delta_y^2) - h^2 M_9(kh)\delta_x^2\delta_y^2\right) \left[(-k^2 - \partial_x^2 - \partial_z^2)^{-1} f\right]_{0,0}. \tag{2.79}$$

The right hand side of Equation (2.79) is a discrete source term that produces a numerical solution that exactly matches with the analytic solution.

When $\operatorname{Im} k > 0$, we know that the impulse response (Green's function) for $f(x, y) = \alpha_{0,0}\delta(x - x_0, y - y_0)$ is expressed as the 0th order Hankel function of the first kind

$$(-k^2 - \partial_x^2 - \partial_z^2)^{-1} f = \frac{i}{4} H_0^{(1)}(kr)\alpha_{0,0}, \tag{2.80}$$

where $r = \sqrt{(x - x_0)^2 + (y - y_0)^2}$ and $H_0^{(1)}(z) = J_0(z) + iY_0(z)$. Then, the right hand side of Equation (2.79) is expressed as

$$\left(-\frac{L_9(kh)}{h^2} - (\delta_x^2 + \delta_y^2) - h^2 M_9(kh)\delta_x^2\delta_y^2\right)\left[\frac{i}{4} H_0^{(1)}(kr)\alpha_{0,0}\right]_{0,0}. \tag{2.81}$$

However, the Hankel function has the logarithmic singularity at $r = 0$, so the computation with the discrete Helmholtz operator does not give an expression with a finite value. Thus, we replace the value at $r = 0$ with the value at $r = h\epsilon > 0$. Equation (2.81) becomes

$$\begin{aligned}
&\left(-\frac{L_9(kh)}{h^2} - (\delta_x^2 + \delta_y^2) - h^2 M_9(kh)\delta_x^2\delta_y^2\right)\left[\frac{i}{4} H_0^{(1)}(kr)\alpha_{0,0}\right]_{0,0} \\
&\quad \approx \frac{i}{4}(-L_9(kh)H_0^{(1)}(kh\epsilon) - (4H_0^{(1)}(kh) - 4H_0^{(1)}(kh\epsilon)) \\
&\qquad\qquad -M_9(kh)(4H_0^{(1)}(\sqrt{2}kh) - 8H_0^{(1)}(kh) + 4H_0^{(1)}(kh\epsilon)))\frac{\alpha_{0,0}}{h^2}
\end{aligned} \tag{2.82}$$

with the finite volume approximation of the 2D impulse source given as

$$\frac{\alpha_{0,0}}{h^2} = \frac{\displaystyle\int_{y_0-\frac{h}{2}}^{y_0+\frac{h}{2}} \int_{x_0-\frac{h}{2}}^{x_0+\frac{h}{2}} \alpha_{0,0}\delta(x - x_0, y - y_0)\,\mathrm{d}x\,\mathrm{d}y}{\displaystyle\int_{y_0-\frac{h}{2}}^{y_0+\frac{h}{2}} \int_{x_0-\frac{h}{2}}^{x_0+\frac{h}{2}} \mathrm{d}x\,\mathrm{d}y}, \tag{2.83}$$

thus, the source amplitude correction function $F_9(kh)$ for the 9-point case is

given as

$$F_9(kh) = \frac{i}{4}(-L_9(kh)H_0^{(1)}(kh\epsilon) - (4H_0^{(1)}(kh) - 4H_0^{(1)}(kh\epsilon)) \\ - M_9(kh)(4H_0^{(1)}(\sqrt{2}kh) - 8H_0^{(1)}(kh) + 4H_0^{(1)}(kh\epsilon))). \tag{2.84}$$

Here, we need to impose a condition for the source correction function to determine ϵ. The source correction function should be 1 with $kh \to 0$ as with $\mathrm{sinc}(kh)$. The requirement can be met by computing ϵ with the limit

$$\lim_{kh\to 0} F_9(kh) = \frac{\log 2 - 10\log\epsilon}{6\pi} = 1, \tag{2.85}$$

thus $\epsilon = \exp((\log 2 - 6\pi)/10) \approx 0.1627$. Because we fully determined $F_9(kh)$, the 9-point discrete Helmholtz equation with the impulse source can be approximated as

$$-\frac{L_9(kh)}{h^2}u_{0,0} - (\delta_x^2 + \delta_y^2)u_{0,0} - h^2 M_9(kh)\delta_x^2\delta_y^2 u_{0,0} = F_9(kh)\frac{\alpha_{0,0}}{h^2}, \tag{2.86}$$

or

$$-\frac{L_9(kh)}{h^2}u_{0,0} - (\delta_x^2 + \delta_y^2)u_{0,0} - h^2\delta_x\delta_y M_9(kh)\delta_x\delta_y u_{0,0} = F_9(kh)\frac{\alpha_{0,0}}{h^2}, \tag{2.87}$$

which comes from the symmetric modification (Equation (2.50)).

The introduction of ϵ is not just simple approximation. Because the numerical solution obtained from the impulse source cannot embed the true singularity of the Hankel function at $r = 0$, so it should give a finite value at $r = 0$. ϵ has a role in removing the singularity in the numerical solution and it approximately predicts the finite value at the singularity. In Chapter 3, we can verify that the numerical solution at the singularity $r = 0$ for the unit impulse source is given as $\frac{i}{4}H_0^{(1)}(kh\epsilon)$.

Although the source amplitude correction is not essential for the 5-point method in Section 2.3.1 because of the limited wavenumber range, the source amplitude correction function for the 5-point method can be obtained as follows

$$\begin{aligned}&\left(-\frac{4-4J_0(kh)}{h^2}-(\delta_x^2+\delta_y^2)\right)\left[\frac{i}{4}H_0^{(1)}(kr)\alpha_{0,0}\right]_{0,0}\\&\approx i(J_0(kh)H_0^{(1)}(kh\epsilon)-H_0^{(1)}(kh))\frac{\alpha_{0,0}}{h^2}\end{aligned}\tag{2.88}$$

and

$$\lim_{kh\to 0}F_5(kh)=\lim_{kh\to 0}i(J_0(kh)H_0^{(1)}(kh\epsilon)-H_0^{(1)}(kh))=-\frac{2\log\epsilon}{\pi}=1,\tag{2.89}$$

which gives $\epsilon=\exp(-\pi/2)\approx 0.2079$.

$F_5(kh)$ and $F_9(kh)$ are shown in Figure 2.6. We can see that the imaginary parts of $F_5(kh)$ and $F_9(kh)$ are relatively small, and $F_9(kh)$ is quite similar to $\mathrm{sinc}(kh)$.

We may compute the series expansion of $F_9(kh)$ as a correction term instead of directly evaluating $F_9(kh)$, because $F_9(kh)$ contains the Hankel functions, which may be cumbersome to numerically evaluate. The series is approximated as

$$\begin{aligned}F_9(kh)\approx{}&1-0.163691940555019(kh)^2+0.00894105617680320 5(kh)^4\\&-0.000283100927590419 3(kh)^6+7.233616285328642\times 10^{-6}(kh)^8\\&-1.2750088335092805\times 10^{-7}(kh)^{10}.\end{aligned}\tag{2.90}$$

The series approximation originally contains imaginary coefficients and log terms, but they are ignored because of their small contribution as shown in Figure 2.6(b). This series approximation can be efficiently computed by the

Horner's rule (Horner, 1819). Figure 2.7 shows that the series expression matches quite well with $\mathrm{Re}(F_9(kh))$.

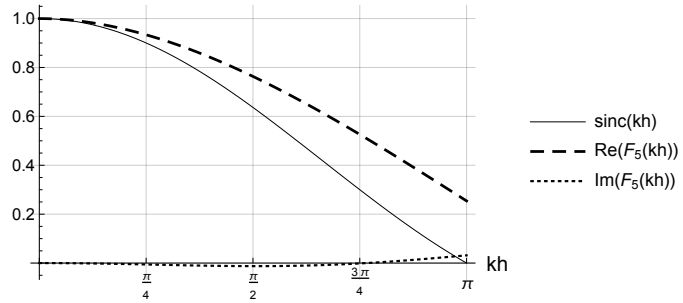

(a) The real and imaginary parts of the source correction function $F_5(kh)$.

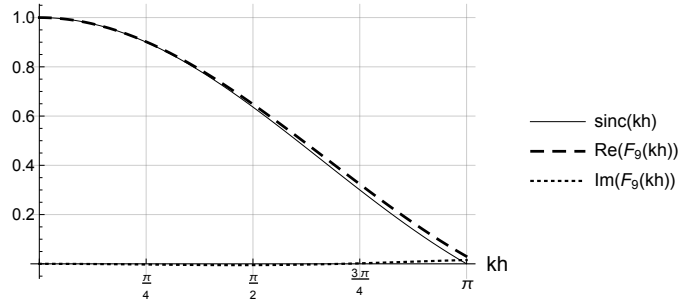

(b) The real and imaginary parts of the source correction function $F_9(kh)$. $F_9(kh)$ is quite similar to $\mathrm{sinc}(kh)$.

Figure 2.6: Source amplitude correction functions for the 2D impulse source.

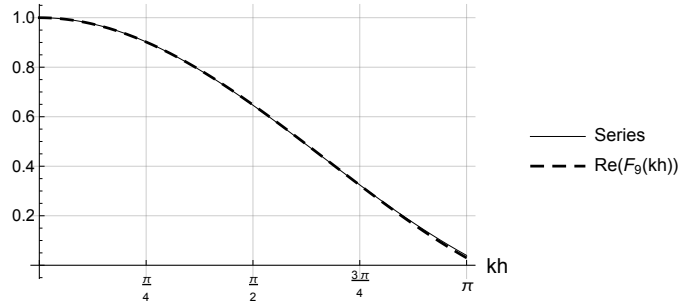

Figure 2.7: The series approximation of $F_9(kh)$. The imaginary coefficients and log terms are omitted in the series approximation.

2.5.3 3D Source Amplitude Correction Functions

The source amplitude correction function for the 3D 7-point method is computed first. The 3D analytic solution for the source $f(x,y,z) = \alpha_{0,0,0}\delta(x - x_0, y - y_0, z - z_0)$ is given as

$$(-k^2 - \partial_x^2 - \partial_y^2 - \partial_z^2)^{-1} f = \frac{e^{ikr}}{4\pi r}\alpha_{0,0,0}, \tag{2.91}$$

where $r = \sqrt{(x-x_0)^2 + (y-y_0)^2 + (z-z_0)^2}$. The singularity at $r = 0$ can be avoided by replacing the value at $r = 0$ with the value at $r = h\epsilon > 0$ as follows

$$\begin{aligned}
&\left(-\frac{6 - 6j_0(kh)}{h^2} - (\delta_x^2 + \delta_y^2 + \delta_z^2)\right)\left[\frac{e^{ikr}}{4\pi r}\alpha_{0,0,0}\right]_{0,0,0} \\
&\approx \left(-\frac{6 - 6j_0(kh)}{h^2}\frac{e^{ikh\epsilon}}{4\pi h\epsilon} - \frac{6}{h^2}\left(\frac{e^{ikh}}{4\pi h} - \frac{e^{ikh\epsilon}}{4\pi h\epsilon}\right)\right)\alpha_{0,0,0} \\
&= \frac{6}{4\pi}\left(\frac{1}{\epsilon}e^{ikh\epsilon}j_0(kh) - e^{ikh}\right)\frac{\alpha_{0,0,0}}{h^3}
\end{aligned} \tag{2.92}$$

with the finite volume approximation of the impulse source

$$\frac{\alpha_{0,0,0}}{h^3} = \frac{\displaystyle\int_{z_0-\frac{h}{2}}^{z_0+\frac{h}{2}}\int_{y_0-\frac{h}{2}}^{y_0+\frac{h}{2}}\int_{x_0-\frac{h}{2}}^{x_0+\frac{h}{2}} \alpha_{0,0,0}\delta(x - x_0, y - y_0, z - z_0)\,\mathrm{d}x\,\mathrm{d}y\,\mathrm{d}z}{\displaystyle\int_{z_0-\frac{h}{2}}^{z_0+\frac{h}{2}}\int_{y_0-\frac{h}{2}}^{y_0+\frac{h}{2}}\int_{x_0-\frac{h}{2}}^{x_0+\frac{h}{2}} \mathrm{d}x\,\mathrm{d}y\,\mathrm{d}z}. \tag{2.93}$$

Thus, the source correction function for the 7-point method can be expressed as

$$F_7(kh) = \frac{3}{2\pi}\left(\frac{1}{\epsilon}\exp(ikh\epsilon)j_0(kh) - \exp(ikh)\right). \tag{2.94}$$

The limit of $F_7(kh)$ has the following expression

$$\lim_{kh\to 0} F_7(kh) = \frac{3 - 3\epsilon}{2\pi\epsilon} = 1, \tag{2.95}$$

thus $\epsilon = 3/(3+2\pi) \approx 0.3232$.

We can also apply the singularity removal process to the 19-point case.

$$\begin{aligned}
&\left(-\frac{L_{19}(kh)}{h^2} - (\delta_x^2+\delta_y^2+\delta_z^2) - h^2 M_{19}(kh)(\delta_x^2\delta_y^2+\delta_y^2\delta_z^2+\delta_z^2\delta_x^2)\right)\left[\frac{e^{ikr}}{4\pi r}\alpha_{0,0,0}\right]_{0,0,0} \\
\approx &\left(-L_{19}(kh)\frac{e^{ikh\epsilon}}{4\pi\epsilon} - 6\left(\frac{e^{ikh}}{4\pi} - \frac{e^{ikh\epsilon}}{4\pi\epsilon}\right)\right. \\
&\left. - M_{19}(kh)\left(-\frac{24e^{ikh}}{4\pi} + \frac{12e^{i\sqrt{2}kh}}{4\pi\sqrt{2}} + \frac{12e^{ikh\epsilon}}{4\pi\epsilon}\right)\right)\frac{\alpha_{0,0,0}}{h^3}
\end{aligned} \tag{2.96}$$

Thus, the source correction function for the 19-point case is defined as

$$\begin{aligned}
F_{19}(kh) = &-L_{19}(kh)\frac{e^{ikh\epsilon}}{4\pi\epsilon} - 6\left(\frac{e^{ikh}}{4\pi} - \frac{e^{ikh\epsilon}}{4\pi\epsilon}\right) \\
&- M_{19}(kh)\left(-\frac{24e^{ikh}}{4\pi} + \frac{12e^{i\sqrt{2}kh}}{4\pi\sqrt{2}} + \frac{12e^{ikh\epsilon}}{4\pi\epsilon}\right),
\end{aligned} \tag{2.97}$$

and the limit of $F_{19}(kh)$ has the following form

$$\lim_{kh\to 0} F_{19}(kh) = \frac{4-(2+\sqrt{2})\epsilon}{4\pi\epsilon} = 1, \tag{2.98}$$

thus $\epsilon = 4/(2+\sqrt{2}+4\pi) \approx 0.2503$.

Also, we apply the singularity removal process to the 27-point case as follows

$$\begin{aligned}
&\left(-\frac{L_{27}(kh)}{h^2} - (\delta_x^2+\delta_y^2+\delta_z^2)\right. \\
&\left. - h^2 M_{27}(kh)(\delta_x^2\delta_y^2+\delta_y^2\delta_z^2+\delta_z^2\delta_x^2) - h^4 N_{27}(kh)\delta_x^2\delta_y^2\delta_z^2\right)\left[\frac{e^{ikr}}{4\pi r}\alpha_{0,0,0}\right]_{0,0,0} \\
\approx &\left(-L_{27}(kh)\frac{e^{ikh\epsilon}}{4\pi\epsilon} - 6\left(\frac{e^{ikh}}{4\pi} - \frac{e^{ikh\epsilon}}{4\pi\epsilon}\right)\right. \\
&- M_{27}(kh)\left(-\frac{24e^{ikh}}{4\pi} + \frac{12e^{i\sqrt{2}kh}}{4\pi\sqrt{2}} + \frac{12e^{ikh\epsilon}}{4\pi\epsilon}\right) \\
&\left. - N_{27}(kh)\left(\frac{24e^{ikh}}{4\pi} - \frac{24e^{i\sqrt{2}kh}}{4\pi\sqrt{2}} + \frac{8e^{i\sqrt{3}kh}}{4\pi\sqrt{3}} - \frac{8e^{ikh\epsilon}}{4\pi\epsilon}\right)\right)\frac{\alpha_{0,0,0}}{h^3}.
\end{aligned} \tag{2.99}$$

The source amplitude correction function for the 27-point case is expressed as

$$\begin{aligned} F_{27}(kh) = &- L_{27}(kh)\frac{e^{ikh\epsilon}}{4\pi\epsilon} - 6\left(\frac{e^{ikh}}{4\pi} - \frac{e^{ikh\epsilon}}{4\pi\epsilon}\right) \\ &- M_{27}(kh)\left(-\frac{24e^{ikh}}{4\pi} + \frac{12e^{i\sqrt{2}kh}}{4\pi\sqrt{2}} + \frac{12e^{ikh\epsilon}}{4\pi\epsilon}\right) \\ &- N_{27}(kh)\left(\frac{24e^{ikh}}{4\pi} - \frac{24e^{i\sqrt{2}kh}}{4\pi\sqrt{2}} + \frac{8e^{i\sqrt{3}kh}}{4\pi\sqrt{3}} - \frac{8e^{ikh\epsilon}}{4\pi\epsilon}\right), \end{aligned} \tag{2.100}$$

and the limit of $F_{27}(kh)$ has the following expression

$$\lim_{kh\to 0} F_{27}(kh) = \frac{192 - (126 + 27\sqrt{2} + 4\sqrt{3})\epsilon}{180\pi\epsilon} = 1, \tag{2.101}$$

thus $\epsilon = 192/(126 + 27\sqrt{2} + 4\sqrt{3} + 180\pi) \approx 0.2607$. Then, the 27-point discrete expression with the impulse source can be expressed as

$$\begin{aligned} -\frac{L_{27}(kh)}{h^2}u_{0,0,0} - (\delta_x^2 + \delta_y^2 + \delta_z^2)u_{0,0,0} - h^2\delta_x\delta_y M_{27}(kh)\delta_x\delta_y u_{0,0,0} \\ -h^2\delta_y\delta_z M_{27}(kh)\delta_y\delta_z u_{0,0,0} \\ -h^2\delta_z\delta_x M_{27}(kh)\delta_z\delta_x u_{0,0,0} \\ -h^4\delta_x\delta_y\delta_z N_{27}(kh)\delta_x\delta_y\delta_z u_{0,0,0} = F_{27}(kh)\frac{\alpha_{0,0,0}}{h^3}, \end{aligned} \tag{2.102}$$

which comes from the symmetric modification Equation (2.69).

All the source amplitude correction functions for the 3D cases are shown in Figure 2.8.

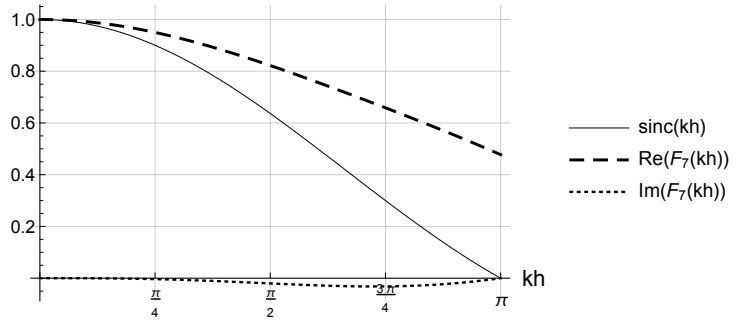

(a) The real and imaginary parts of the source correction function $F_7(kh)$ for the 7-point method

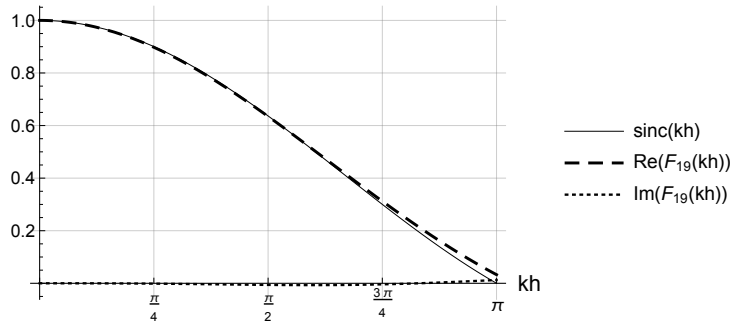

(b) The real and imaginary parts of the source correction function $F_{19}(kh)$ for the 19-point method. $F_{19}(kh)$ is quite similar to $\mathrm{sinc}(kh)$.

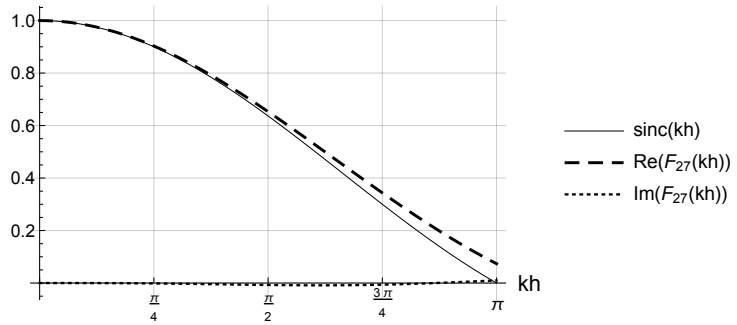

(c) The real and imaginary parts of the source correction function $F_{27}(kh)$ for the 27-point method. $F_{27}(kh)$ slightly deviates from $\mathrm{sinc}(kh)$ when kh becomes large.

Figure 2.8: The source amplitude correction functions for the 3D impulse source.

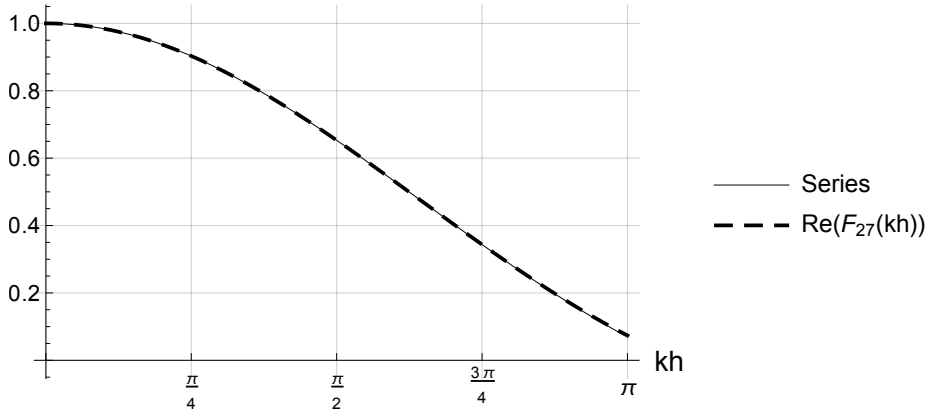

Figure 2.9: The series expression of $F_{27}(kh)$. It matches well with $\mathrm{Re}(F_{27}(kh))$.

To avoid numerical evaluation of the several complex exponential functions and the spherical Bessel functions in $F_{27}(kh)$, we use the following series expression

$$\begin{aligned} F_{27}(kh) \approx\ & 1 - 0.1629235349294909(kh)^2 + 0.010029553652376767(kh)^4 \\ & - 0.0004383253850535262(kh)^6 + 0.00001684211345513565(kh)^8 \\ & - 4.0663798991259547 \times 10^{-7}(kh)^{10}, \end{aligned} \tag{2.103}$$

which can be efficiently evaluated by the Horner's rule (Horner, 1819). Although $F_{27}(kh)$ contains odd power terms with complex coefficients, they are omitted because of their small contribution as we can see the imaginary part of $F_{27}(kh)$ in Figure 2.8(c). Figure 2.9 shows that $F_{27}(kh)$ and the series are matched well.

Chapter 3

Dispersion Analysis and Numerical Experiments

We examine the accuracy of each finite difference method by means of the plane wave analysis. It is also shown that the proposed methods with the source amplitude correction functions give correct discrete impulse responses matched with the analytic impulse responses. Then, 2D seismic wave propagation in heterogeneous media is briefly examined with the proposed methods.

3.1 Plane Wave Analysis

3.1.1 2D Dispersion Curves

The dispersion characteristic for each finite difference method can be analyzed by the plane wave analysis. If we assume that the numerical solution is a plane wave ansatz $u(x, y) = \exp(i\tilde{k}(\cos(\theta)x + \sin(\theta)y))$ with the numerical wavenum-

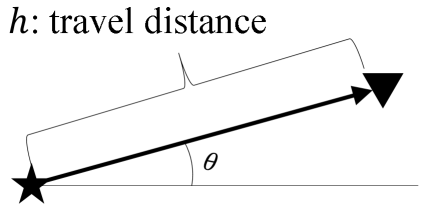

$\exp(ikh)$: actual phase change
$\exp(i\tilde{k}h)$: numerical phase change
$\tilde{k}h - kh$: phase difference in radian
$(\tilde{k}h - kh)/2\pi$: phase difference in cycle

Figure 3.1: A schematic for describing the phase difference when the wave travels distance h with the propagation angle θ

ber $\tilde{k}$, then we obtain $\partial_x u = i\tilde{k}\cos(\theta)u$ and $\partial_y u = i\tilde{k}\sin(\theta)u$. The angle θ for the plane wave direction goes from the positive x-axis to the positive y-axis. For the plane wave solution u, the second order finite difference operators can be written as

$$\begin{aligned} \delta_x^2 u &= \frac{2\cosh(\partial_x h) - 2}{h^2} u \\ &= \frac{2\cos(k_x h) - 2}{h^2} u, \\ \delta_y^2 u &= \frac{2\cos(k_y h) - 2}{h^2} u, \end{aligned} \tag{3.1}$$

where $k_x h = \tilde{k}h\cos(\theta)$ and $k_y h = \tilde{k}h\sin(\theta)$. Using these relations, we can rewrite finite difference equations with the numerical dispersion relation in terms of kh and $\tilde{k}h$. We will treat the dimensionless quantity kh as a whole. It also applies to $\tilde{k}h$.

Using the plane wave assumption, we compare our proposed scheme with the previous works introduced in Chapter 1 as follows:

Naïve 2nd order method

Inserting Equation (3.1) into the naïve second order method, we can obtain the following numerical dispersion relation

$$-(kh)^2 - ((2\cos(k_x h) - 2) + (2\cos(k_y h) - 2)) = 0, \tag{3.2}$$

and kh can be explicitly expressed as

$$kh = \sqrt{-((2\cos(k_x h) - 2) + (2\cos(k_y h) - 2))}, \tag{3.3}$$

which is a function of $\tilde{k}h$ and θ. When the wave travels distance h, kh and $\tilde{k}h$ are the actual phase change and the numerical phase change, respectively. We can take $(\tilde{k}h - kh)/2\pi$ as an error measure which has the unit *cycle* and the difference should be as small as possible. In Figure 3.2, the phase difference of the naïve finite difference method is plotted for various $\tilde{k}h$ and uniformly divided propagation angles in the range of $0 \leq \theta \leq \pi/4$ (because of symmetry).

Nehrbass et al. (1998)'s 2nd order method

From Equation (2.37), we can obtain the following equation

$$-(4 - 4J_0(kh)) - ((2\cos(k_x h) - 2) + (2\cos(k_y h) - 2)) = 0. \tag{3.4}$$

Because of $J_0(kh)$, kh cannot be expressed explicitly. We can solve kh for given $\tilde{k}h$ by using iterative root finding methods. The phase difference is shown in Figure 3.3.

Jo et al. (1996)'s 9-point method

This method reduces the dispersion error by optimization without increasing

the order of accuracy, and the method remains second order of accuracy. The equation for computing the dispersion error is expressed as

$$\begin{aligned} &-(kh)^2\left(c+\frac{1-c}{4}(2\cos(k_xh)+2\cos(k_yh))\right) \\ &-((2\cos(k_xh)-2)+(2\cos(k_yh)-2)) \\ &-\frac{1-a}{2}(2\cos(k_xh)-2)(2\cos(k_yh)-2)=0, \end{aligned} \tag{3.5}$$

where a and c are optimized weighting parameters. The coefficients a and c originally derived in Jo et al. (1996) are 0.5461 and 0.6248, respectively. We recomputed the coefficients from optimization using an objective function with the phase difference $(\tilde{k}h - kh)/2\pi$. We obtained $a = 0.5713$ and $b = 0.6274$, and they give slightly smaller phase difference errors than those of Jo et al. (1996). The phase difference is shown in Figure 3.4.

Singer and Turkel (1998)'s 4th order method

This 4th order method also utilize the 9-point stencil. The numerical dispersion relation between kh and $\tilde{k}h$ is expressed as

$$\begin{aligned} -\left((kh)^2-\frac{(kh)^4}{12}\right)-((2\cos(k_xh)-2)+(2\cos(k_yh)-2)) \\ -\frac{1}{6}(2\cos(k_xh)-2)(2\cos(k_yh)-2)=0. \end{aligned} \tag{3.6}$$

The phase difference is shown in Figure 3.5.

6th order method

The 6th order method (Singer and Turkel, 2006; Sutmann, 2007; Nabavi et al., 2007) has the following relation

$$\begin{aligned} -L_{6\text{th}}(kh)-((2\cos(k_xh)-2)+(2\cos(k_yh)-2)) \\ -M_{6\text{th}}(kh)(2\cos(k_xh)-2)(2\cos(k_yh)-2)=0 \end{aligned} \tag{3.7}$$

where $L_{6\text{th}}(kh) = (kh)^2 - (kh)^4/12 + (kh)^6/360$ and $M_{6\text{th}}(kh) = 1/6 + (kh)^2/180$ from Equation (2.71). The 6th order method contains more series terms than Singer and Turkel (1998)'s 4th order method. The phase difference is shown in Figure 3.6.

Tsukerman (2006)'s method

The plane wave basis functions are used in Tsukerman (2006)'s work. The numerical dispersion relation can be expressed as

$$\begin{aligned} &-(2-2\cos(kh)) - ((2\cos(k_x h)-2) + (2\cos(k_y h)-2)) \\ &- \frac{-(2-2\cos(kh)) - (4\cos(kh/\sqrt{2})-4)}{(2\cos(kh/\sqrt{2})-2)^2}(2\cos(k_x h)-2)(2\cos(k_y h)-2) = 0. \end{aligned} \tag{3.8}$$

The phase difference is shown in Figure 3.7.

9-point method of this thesis

The numerical dispersion relation directly comes from Equation (2.46) as follows

$$\begin{aligned} -L_9(kh) - ((2\cos(k_x h)-2) + (2\cos(k_y h)-2)) \\ - M_9(kh)(2\cos(k_x h)-2)(2\cos(k_y h)-2) = 0. \end{aligned} \tag{3.9}$$

The phase difference is shown in Figure 3.8.

We can see that the phase difference (dispersion error) reduces from Figure 3.2 to Figure 3.8. An interesting point of Jo et al. (1996)'s method is that the dispersion error of Jo et al. (1996)'s method is better than that of Singer and Turkel (1998)'s 4th order method if we use approximately the range of $1/G = \tilde{k}h/2\pi > 0.18$.

For easy comparison, we can think of another measure such as

$$\frac{\pi/4}{\max_{\theta}|\tilde{k}h - kh|}. \tag{3.10}$$

The measure is interpreted as the number of grids when the propagated wave reaches the phase difference error of 1/8 cycle ($\pi/4$ radian) in the maximum phase error direction for given $\tilde{k}h$. The measure can be used to roughly determine the size of computational mesh although the measure is not strictly the number of grids if the maximum error direction is not aligned to the coordinate axes. Using the measure, we can estimate the feasible maximum number of grids for numerical simulation for given $\tilde{k}h$ as shown in Figure 3.9. The 9-point method proposed in this thesis has the highest number of grids along $1/G$. In other words, the dispersion error of the 9-point method accumulates less than the other methods.

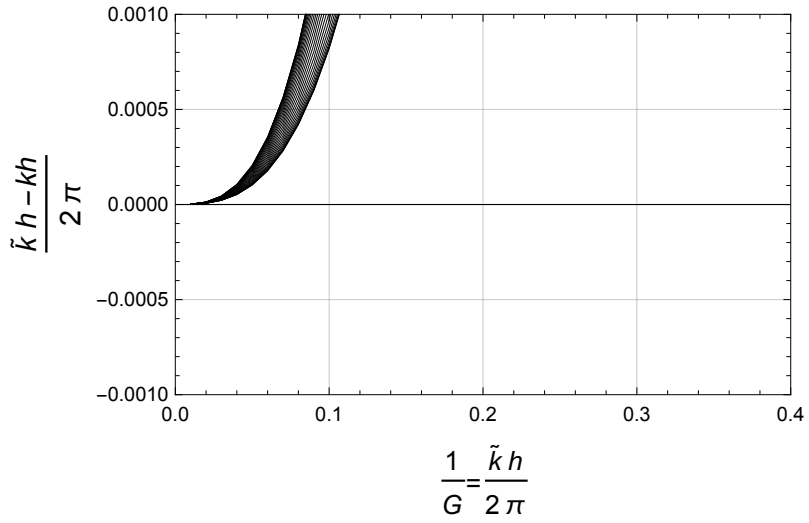

Figure 3.2: Dispersion error curves for the 2D naïve second order method

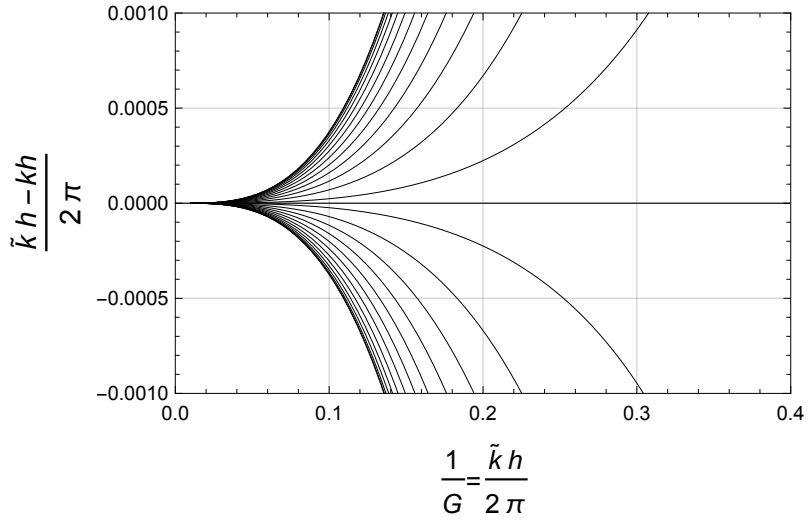

Figure 3.3: Dispersion error curves for Nehrbass et al. (1998)'s 2D second order method

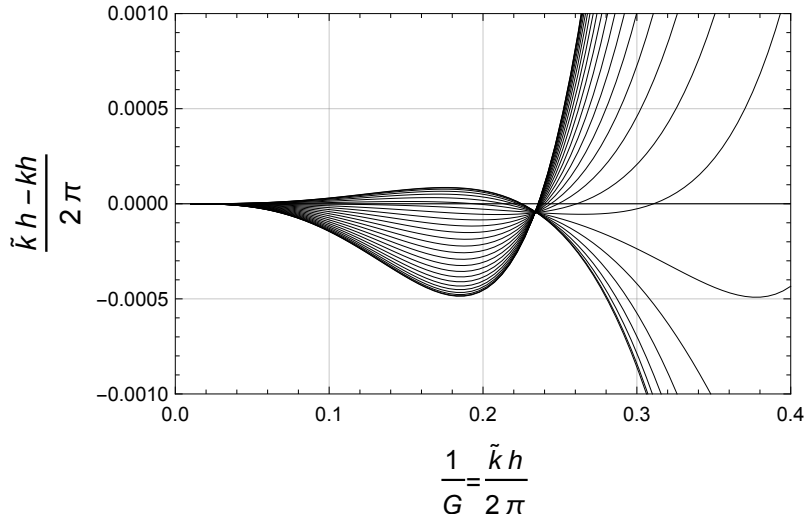

Figure 3.4: Dispersion error curves for Jo et al. (1996)'s method with the modified coefficients a and c

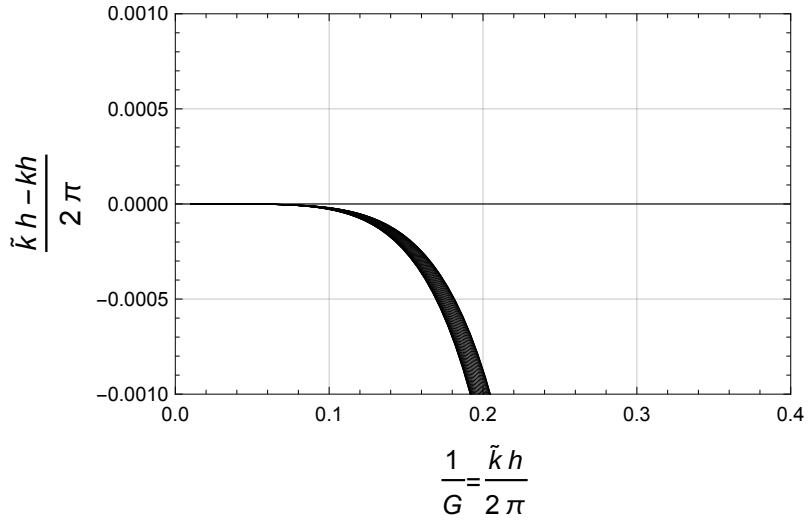

Figure 3.5: Dispersion error curves for Singer and Turkel (1998)'s 2D fourth order method

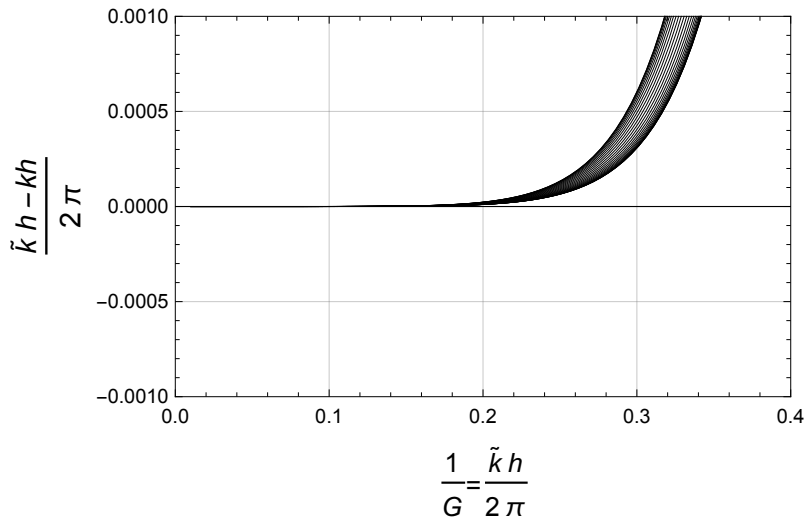

Figure 3.6: Dispersion error curves for the 6th order method (Singer and Turkel, 2006; Sutmann, 2007; Nabavi et al., 2007)

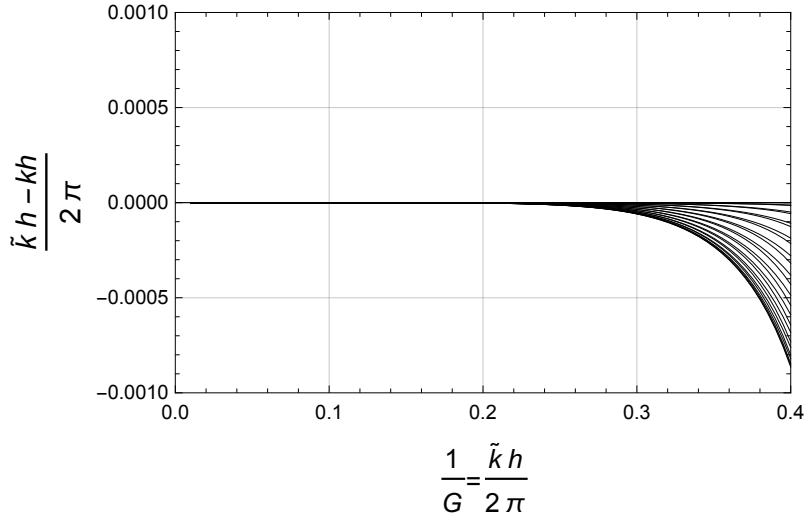

Figure 3.7: Dispersion error curves for Tsukerman (2006)'s method

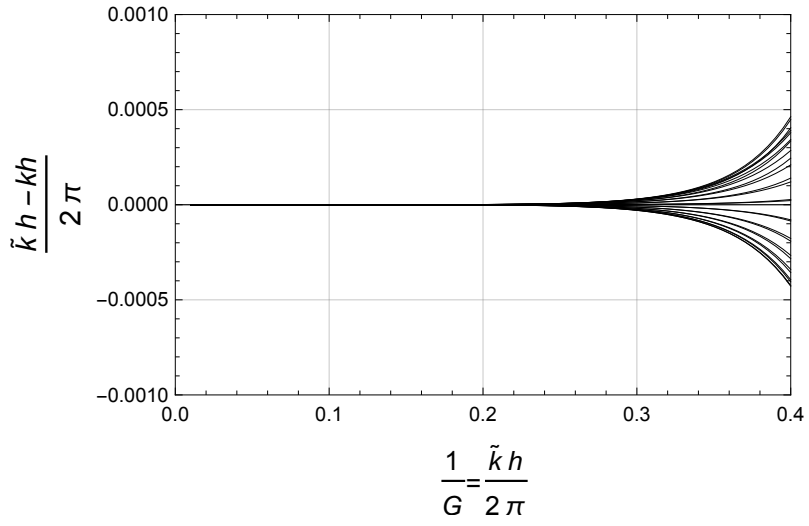

Figure 3.8: Dispersion error curves for the 9-point method of this thesis

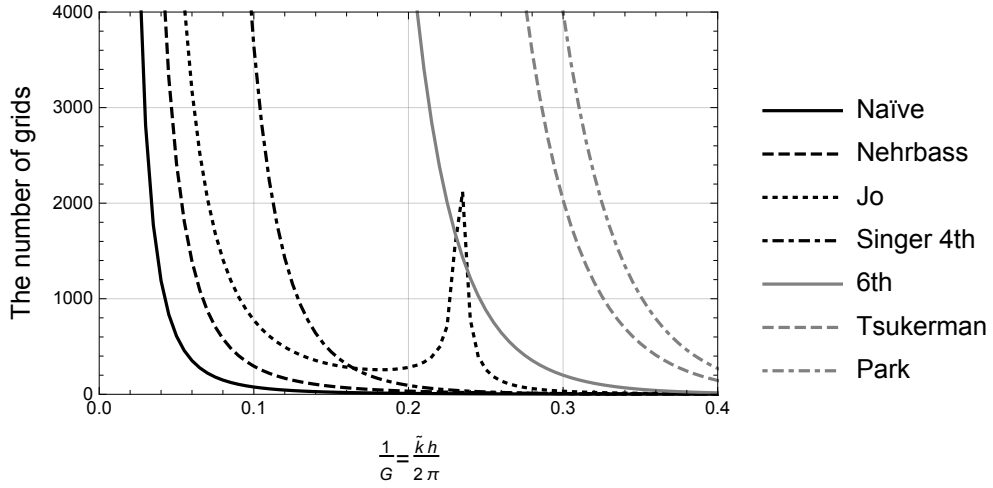

Figure 3.9: The number of grids required to reach 1/8 cycle ($\pi/4$ radian) phase error for 2D methods. Higher is better.

3.1.2 3D Dispersion Curves

From the 3D plane wave ansatz $u(x, y, z) = \exp(i\tilde{k}(\sin(\theta)\cos(\phi)x + \sin(\theta)\sin(\phi)y + \cos(\theta)))$ with the numerical wavenumber $\tilde{k}$, we obtain the following partial derivative relations

$$\begin{aligned} \partial_x u &= i\tilde{k}\sin(\theta)\cos(\phi)u, \\ \partial_y u &= i\tilde{k}\sin(\theta)\sin(\phi)u, \\ \partial_z u &= i\tilde{k}\cos(\theta)u. \end{aligned} \tag{3.11}$$

Thus, the finite difference operators for the plane wave become

$$\begin{aligned} \delta_x^2 u &= \frac{2\cos(k_x h) - 2}{h^2}u, \\ \delta_y^2 u &= \frac{2\cos(k_y h) - 2}{h^2}u, \\ \delta_z^2 u &= \frac{2\cos(k_z h) - 2}{h^2}u, \end{aligned} \tag{3.12}$$

where $k_x h = \tilde{k}h\sin(\theta)\cos(\phi)$, $k_y h = \tilde{k}h\sin(\theta)\sin(\phi)$ and $k_z h = \tilde{k}h\cos(\theta)$. We compute the dispersion curves only for $0 \leq \theta \leq \pi/2$ and $0 \leq \phi \leq \pi/4$ using symmetry. Six compact finite difference methods are compared as follows:

Naïve 2nd order method

The numerical dispersion equation of this method comes directly from Equation (2.11).

$$-(kh)^2 - ((2\cos(k_x h) - 2) + (2\cos(k_y h) - 2) + (2\cos(k_z h) - 2)) = 0 \tag{3.13}$$

The phase difference is shown in Figure 3.10.

Nehrbass et al. (1998)'s 2nd order method

$$-(6-6j_0(kh)) - ((2\cos(k_xh)-2)+(2\cos(k_yh)-2)+(2\cos(k_zh)-2)) = 0 \tag{3.14}$$

The phase difference is shown in Figure 3.11. As with the 2D method of Nehrbass et al. (1998), this method is slightly better than the 3D naïve second order method.

Operto et al. (2007)'s method

Operto et al. (2007) extended Jo et al. (1996)'s approach to the 3D problem.

$$\begin{aligned}
-(kh)^2 \Big(& w_{m1} + \frac{w_{m2}}{6}(2\cos(k_xh)+2\cos(k_yh)+2\cos(k_zh)) \\
& + \frac{w_{m3}}{12}(2\cos(k_xh+k_yh)+2\cos(k_xh-k_yh)+2\cos(k_yh+k_zh) \\
& +2\cos(k_yh-k_zh)+2\cos(k_zh+k_xh)+2\cos(k_zh-k_xh)) \Big) \\
& -\Big((2\cos(k_xh)-2)+(2\cos(k_yh)-2)+(2\cos(k_zh)-2)\Big) \\
-\Big(\frac{w_2}{6}+\frac{w_3}{2}\Big) \Big(& (2\cos(k_xh)-2)(2\cos(k_yh)-2) \\
& +(2\cos(k_yh)-2)(2\cos(k_zh)-2) \\
& +(2\cos(k_zh)-2)(2\cos(k_xh)-2)\Big) \\
& -\frac{3w_3}{8}(2\cos(k_xh)-2)(2\cos(k_yh)-2)(2\cos(k_zh)-2) = 0,
\end{aligned} \tag{3.15}$$

where $w_{m1} = 0.4965$, $w_{m2} = 0.4510$, $w_{m3} = 0.0525$, $w_2 = 0.8901$ and $w_3 = 0.1099$. The phase difference is shown in Figure 3.12.

19-point method of this thesis

The phase difference is shown in Figure 3.13 for the following numerical dispersion relation

$$\begin{aligned}
-L_{19}(kh) - \Big((2\cos(k_x h) - 2) + (2\cos(k_y h) - 2) + (2\cos(k_z h) - 2)\Big) \\
-M_{19}(kh)\Big((2\cos(k_x h) - 2)(2\cos(k_y h) - 2) \\
+(2\cos(k_y h) - 2)(2\cos(k_z h) - 2) \\
+(2\cos(k_z h) - 2)(2\cos(k_x h) - 2)\Big) = 0.
\end{aligned} \tag{3.16}$$

Sutmann (2007)'s 6th order method

The phase difference is shown in Figure 3.14 for the following numerical dispersion relation

$$\begin{aligned}
-L_{6\text{th}}(kh) - \Big((2\cos(k_x h) - 2) + (2\cos(k_y h) - 2) + (2\cos(k_z h) - 2)\Big) \\
-M_{6\text{th}}(kh)\Big((2\cos(k_x h) - 2)(2\cos(k_y h) - 2) \\
+(2\cos(k_y h) - 2)(2\cos(k_z h) - 2) \\
+(2\cos(k_z h) - 2)(2\cos(k_x h) - 2)\Big) \\
-N_{6\text{th}}(kh)(2\cos(k_x h) - 2)(2\cos(k_y h) - 2)(2\cos(k_z h) - 2) = 0.
\end{aligned} \tag{3.17}$$

27-point method of this thesis

The phase difference is shown in Figure 3.15 for the following numerical

dispersion relation

$$
\begin{aligned}
&-L_{27}(kh) - \Big((2\cos(k_x h) - 2) + (2\cos(k_y h) - 2) + (2\cos(k_z h) - 2)\Big) \\
&\quad -M_{27}(kh)\Big((2\cos(k_x h) - 2)(2\cos(k_y h) - 2) \\
&\qquad\qquad +(2\cos(k_y h) - 2)(2\cos(k_z h) - 2) \\
&\qquad\qquad +(2\cos(k_z h) - 2)(2\cos(k_x h) - 2)\Big) \\
&\quad -N_{27}(kh)(2\cos(k_x h) - 2)(2\cos(k_y h) - 2)(2\cos(k_z h) - 2) = 0.
\end{aligned}
\tag{3.18}
$$

As in 2D, we use the measure

$$
\frac{\pi/4}{\max\limits_{\theta,\phi}|\tilde{k}h - kh|}, \tag{3.19}
$$

which can be used to identify the feasible maximum number of grids for given $\tilde{k}h$. We can see that the phase difference for the 3D methods reduces from Figure 3.10 to Figure 3.15. The proposed 27-point method has the highest feasible number of grids along $1/G$ as shown in Figure 3.16. When $1/G = 0.3$, for example, the feasible maximum number of grids of the 27-point method is about 2000, but the number of grids of Sutmann (2007)'s method, which is the highest among the other methods, is only about 140. Thus, it shows the superiority of the proposed 27-point method.

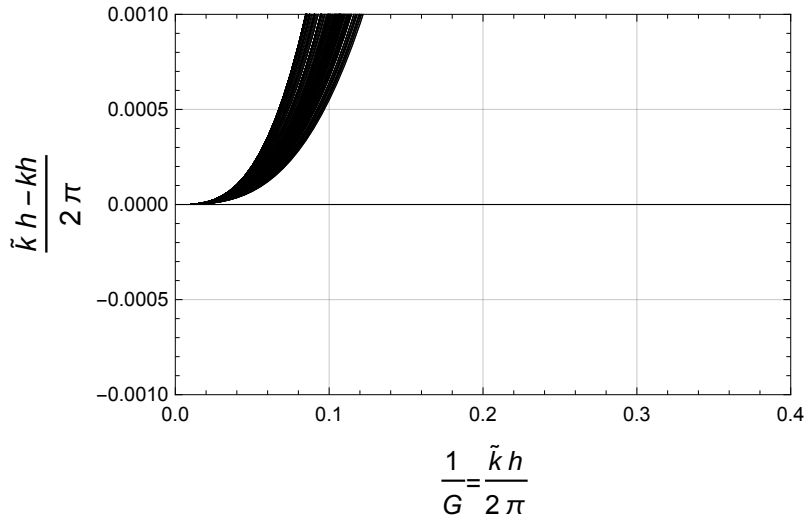

Figure 3.10: Dispersion error curves for the 3D Naïve second order method

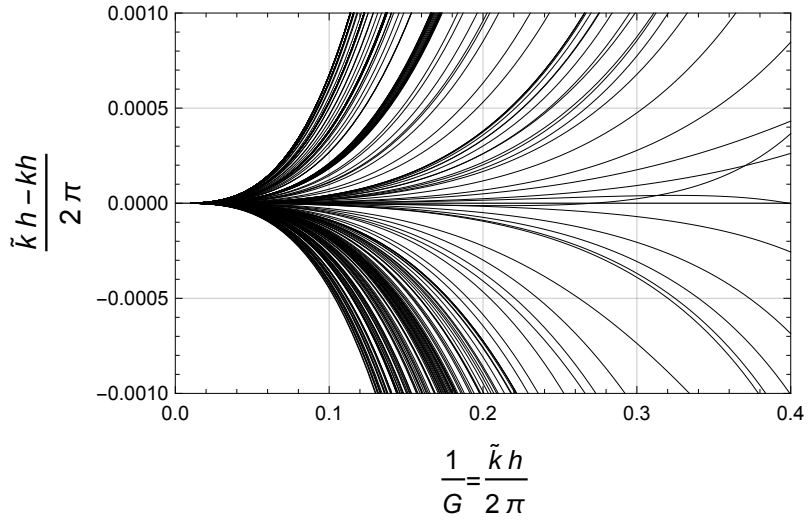

Figure 3.11: Dispersion error curves for Nehrbass et al. (1998)'s 3D second order method

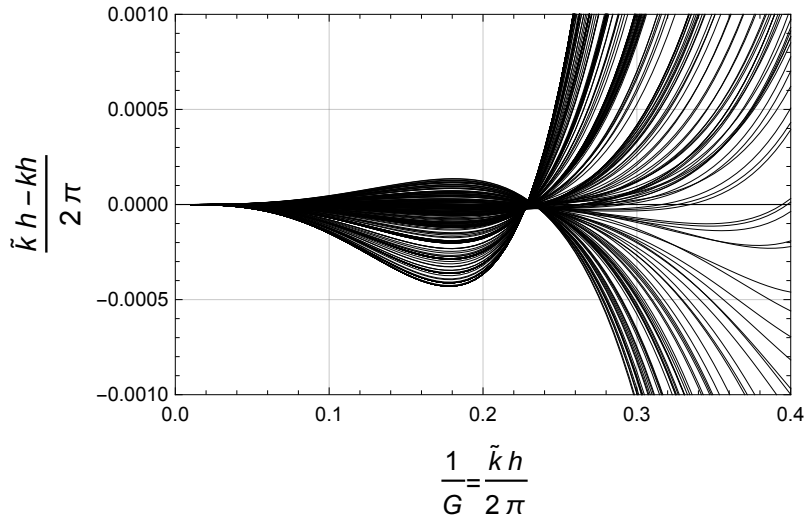

Figure 3.12: Dispersion error curves for Operto et al. (2007)'s method based on Jo et al. (1996)'s approach

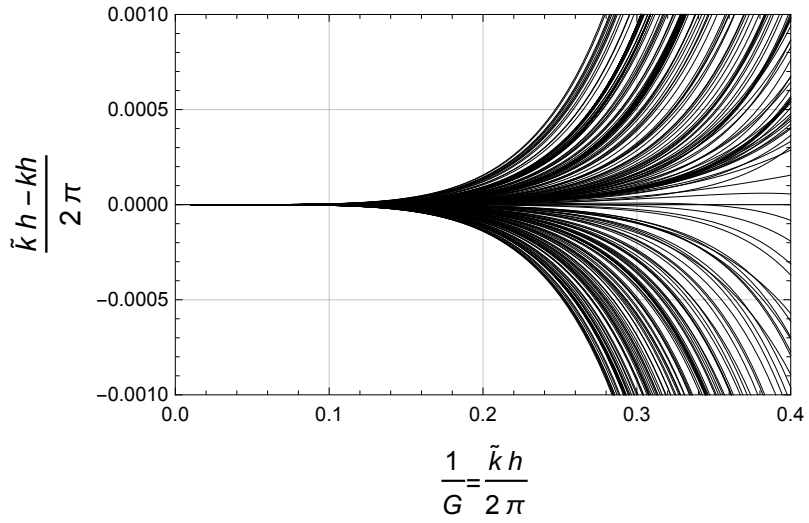

Figure 3.13: Dispersion error curves for the 19-point method of this thesis

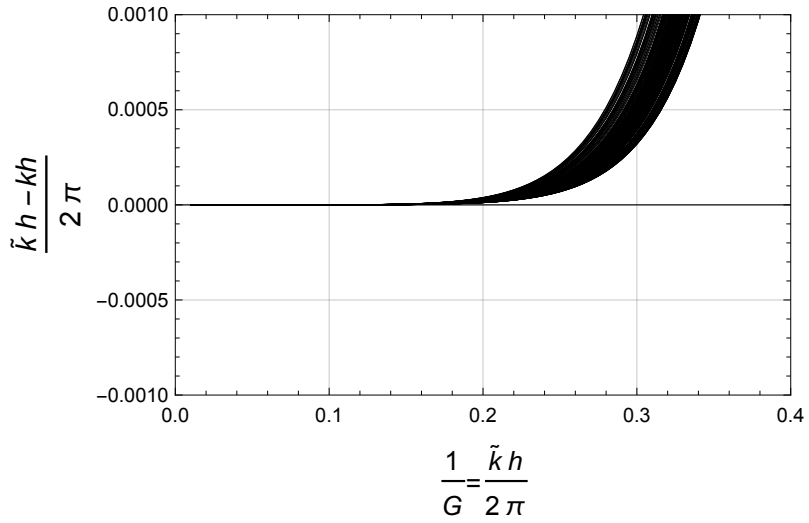

Figure 3.14: Dispersion error curves for Sutmann (2007)'s method

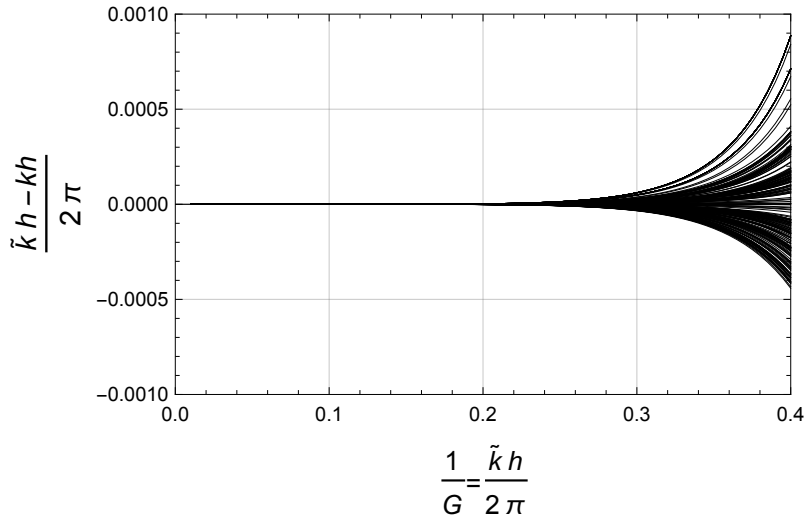

Figure 3.15: Dispersion error curves for the 27-point method of this thesis

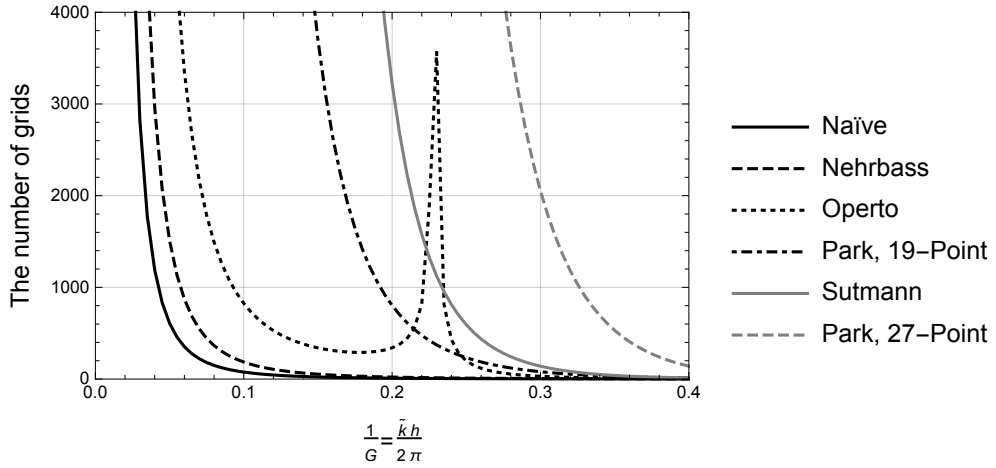

Figure 3.16: The number of grids to reach 1/8 cycle ($\pi/4$ radian) phase error for 3D methods. Higher is better.

3.2 Numerical Solutions with the Impulse Source

All the following numerical experiments use the source amplitude correction functions to compensate the amplitude difference. The numerical solution would not match the analytic solution unless the correction functions are applied.

3.2.1 2D 9-Point Method for a Homogeneous Medium

The numerical solutions were computed by the 9-point method for $\tilde{k}h/2\pi =$ 0.01, 0.10, 0.20, 0.30 and 0.40. Because the 5-point method is not accurate enough to be used in such wide range of $\tilde{k}h$, it was excluded. The size of the 2D computational domain was set to $(n_x \times n_y) = (401 \times 401)$ and the Perfectly Matched Layer (Appendix B) was used for absorbing the outgoing waves. The thickness (the number of grids) of the PML was 20. The unit impulse source was discretized at the exact center node of the computational domain. For $\tilde{k}h/2\pi = 0.30$ and 0.40, the impulse source was approximated also by a set of discrete sources at the 9 neighbor nodes, because the contribution of the neighbor nodes slightly increases when $\tilde{k}h$ is large. Computing the contribution of the neighbor nodes for the impulse source are essentially the same with the process of computing the source amplitude correction functions. The analytic solutions were computed by $\frac{i}{4}H_0^{(1)}(kr)$, and the value at the singular point $r = 0$ in the analytic solution was replaced by $\frac{i}{4}H_0^{(1)}(kh\epsilon)$, which is predicted from the singularity removal process in the previous chapter.

For each $\tilde{k}h$, we extracted a line section parallel to either x- or y-direction, and the line section contains the singularity of the 2D impulse response. From

Figure 3.17 to Figure 3.23, we can see that the discrete and analytic solutions match well together. For $\tilde{k}h/2\pi = 0.30$ and 0.40, we can see that the numerical solutions from the 9-point impulse source approximation are better matched with the predicted value $\frac{i}{4}H_0^{(1)}(kh\epsilon)$ at $r = 0$ than those of the single point approximation. Although Figure 3.24 and Figure 3.25 show that the 9-point approximation of the impulse source is better than the single point approximation in terms of pointwise L_1 error, the single point approximation also works reasonably well.

From the observation above, the source amplitude correction functions and ϵ computed from the singularity removal process are justified. If the source amplitude correction functions are not applied, then the amplitude discrepancy between the numerical solution and the analytic solution would be significant.

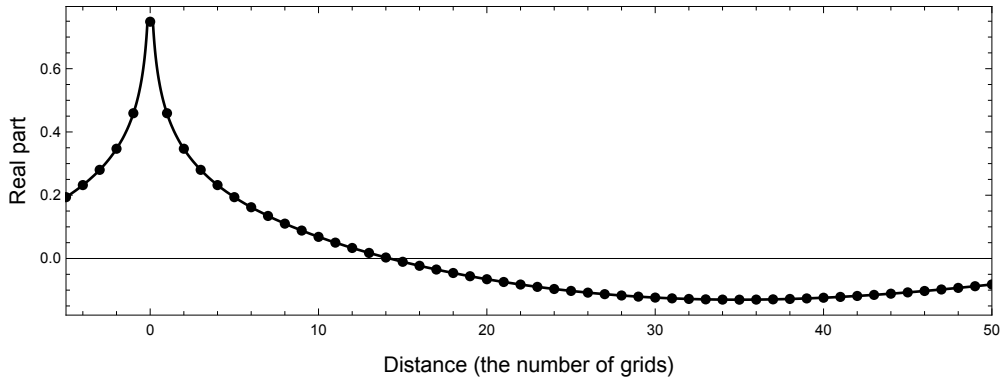

(a) Real part

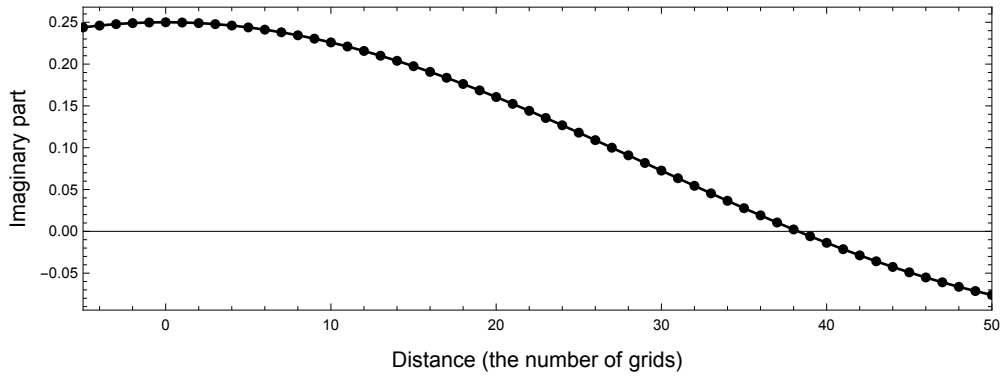

(b) Imaginary part

Figure 3.17: Comparison between the analytic solution (solid line) and the discrete solution (dots) when $1/G = \tilde{k}h/2\pi = 0.01$. The discrete solution is obtained from the proposed 9-point method of this thesis with the single point approximation of the impulse source.

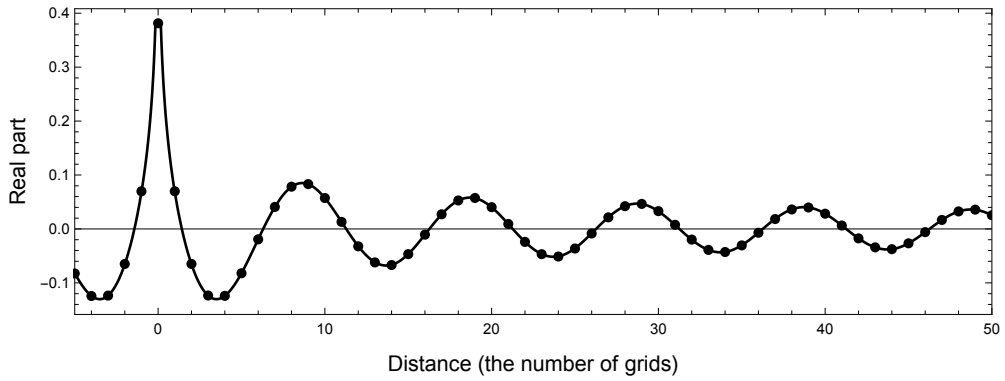

(a) Real part

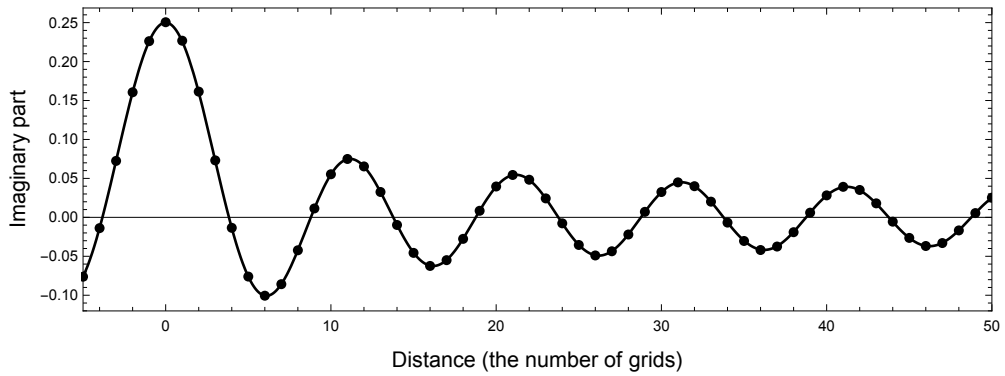

(b) Imaginary part

Figure 3.18: Comparison between the analytic solution (solid line) and the discrete solution (dots) when $1/G = \tilde{k}h/2\pi = 0.10$. The discrete solution is obtained from the proposed 9-point method of this thesis with the single point approximation of the impulse source.

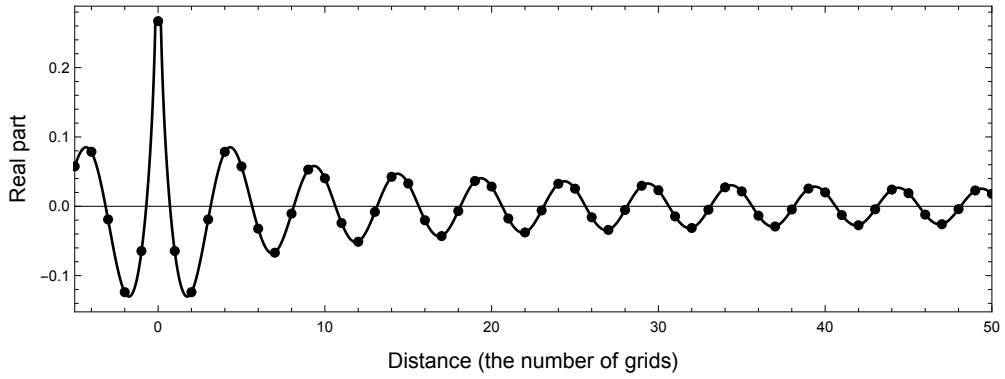

(a) Real part

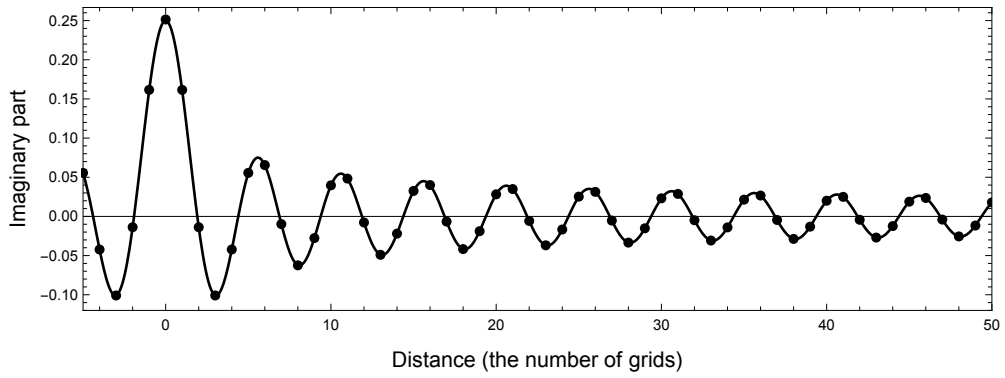

(b) Imaginary part

Figure 3.19: Comparison between the analytic solution (solid line) and the discrete solution (dots) when $1/G = \tilde{k}h/2\pi = 0.20$. The discrete solution is obtained from the proposed 9-point method of this thesis with the single point approximation of the impulse source.

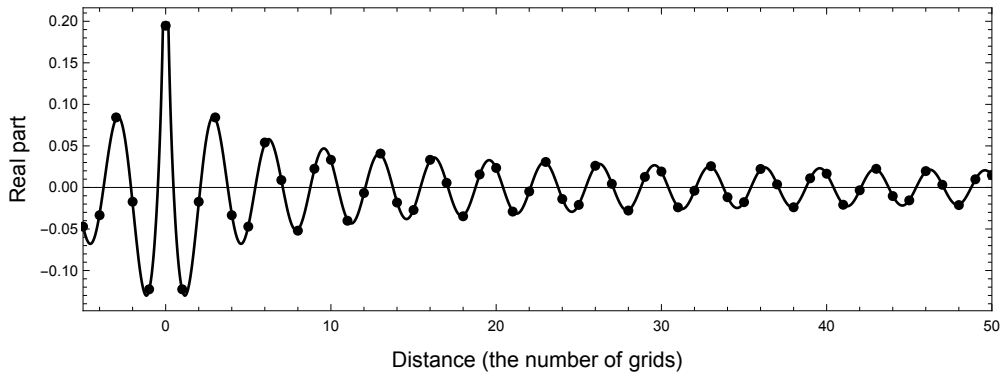

(a) Real part

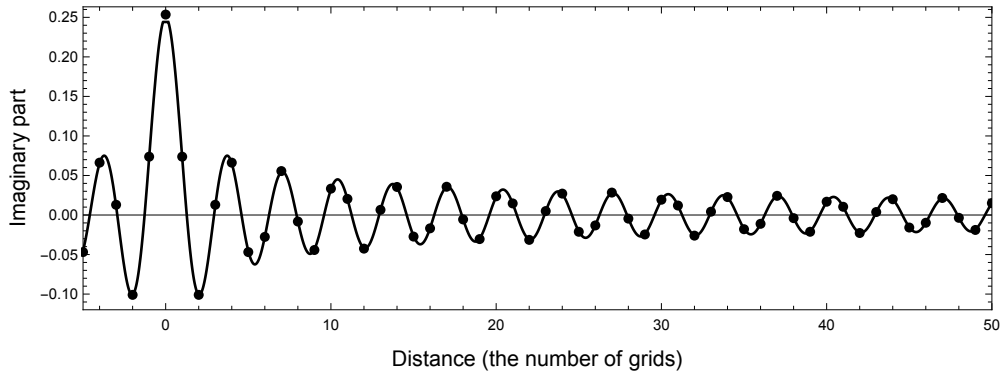

(b) Imaginary part

Figure 3.20: Comparison between the analytic solution (solid line) and the discrete solution (dots) when $1/G = \tilde{k}h/2\pi = 0.30$. The discrete solution is obtained from the proposed 9-point method of this thesis with the single point approximation of the impulse source.

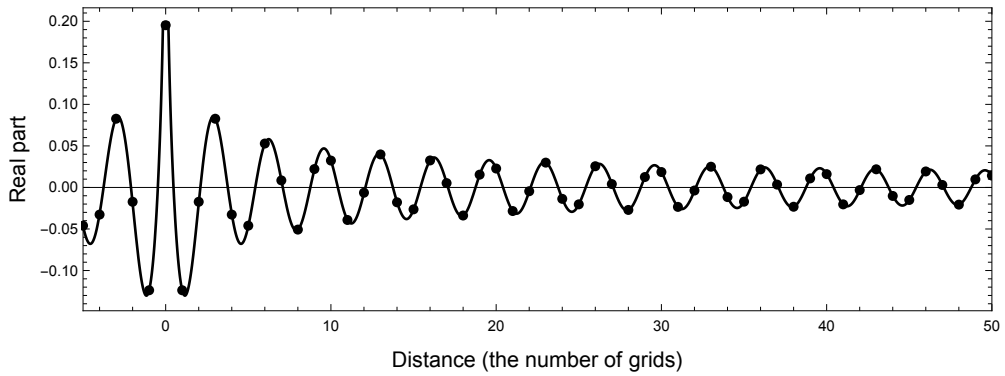

(a) Real part

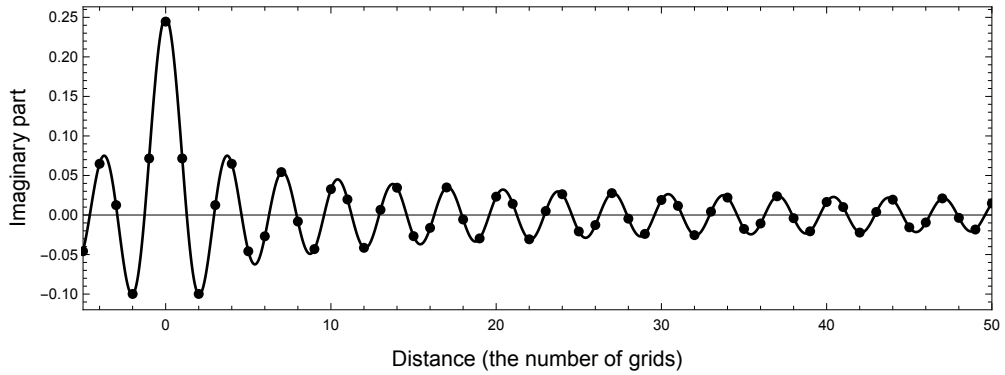

(b) Imaginary part

Figure 3.21: Comparison between the analytic solution (solid line) and the discrete solution (dots) when $1/G = \tilde{k}h/2\pi = 0.30$. The discrete solution is obtained from the proposed 9-point method of this thesis with the 9-point approximation of the impulse source.

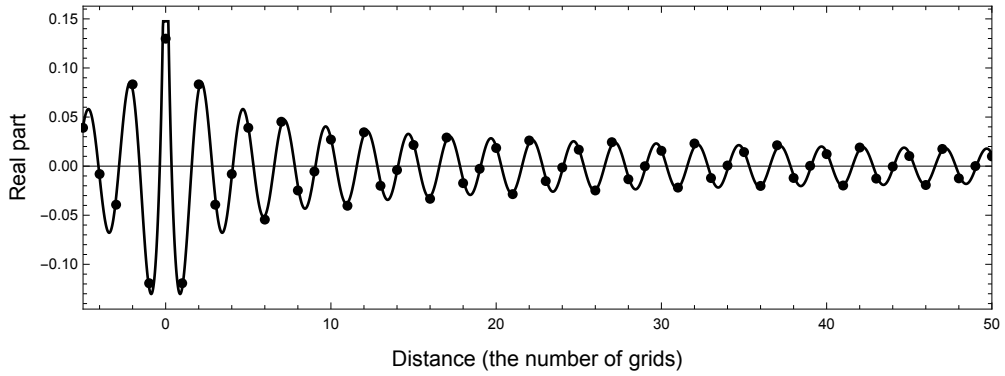

(a) Real part

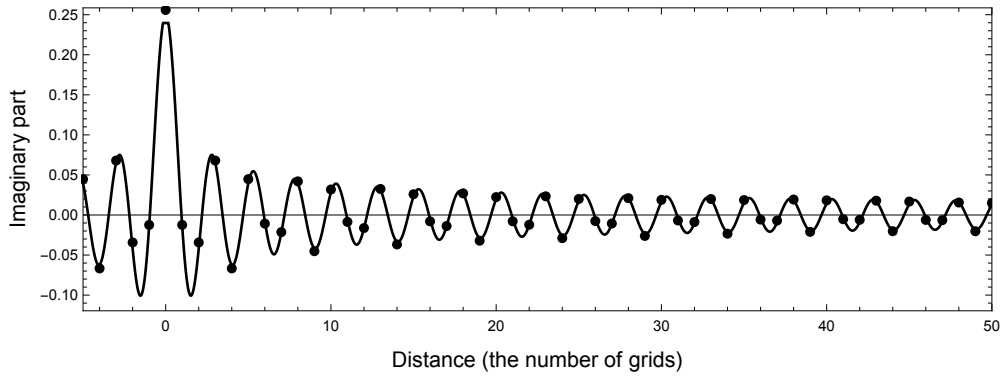

(b) Imaginary part

Figure 3.22: Comparison between the analytic solution (solid line) and the discrete solution (dots) when $1/G = \tilde{k}h/2\pi = 0.40$. The discrete solution is obtained from the proposed 9-point method of this thesis with the single point approximation of the impulse source.

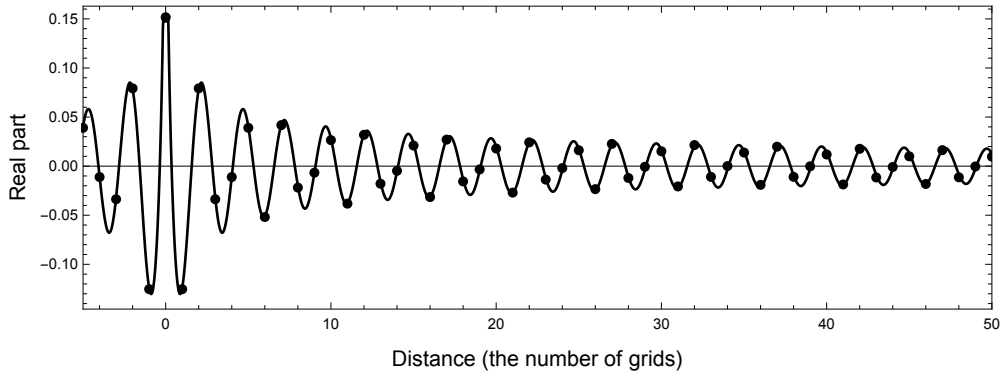

(a) Real part

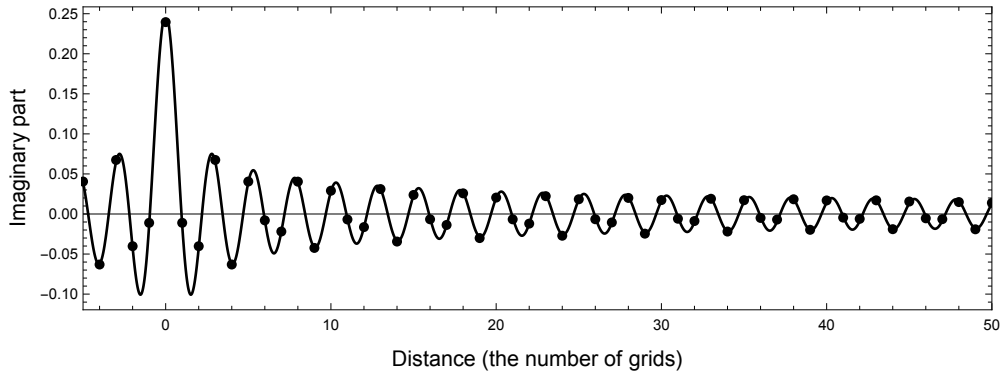

(b) Imaginary part

Figure 3.23: Comparison between the analytic solution (solid line) and the discrete solution (dots) when $1/G = \tilde{k}h/2\pi = 0.40$. The discrete solution is obtained from the proposed 9-point method of this thesis with the 9-point approximation of the impulse source.

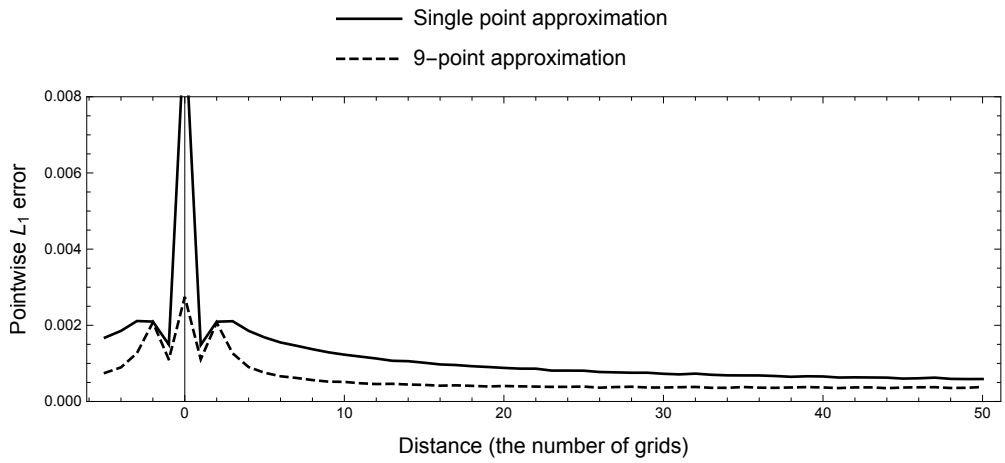

Figure 3.24: Pointwise L_1 error plot for $1/G = \tilde{k}h/2\pi = 0.30$. The solid line is computed from the single point approximation, and the dashed line is computed from the 9 point approximation of the impulse sources.

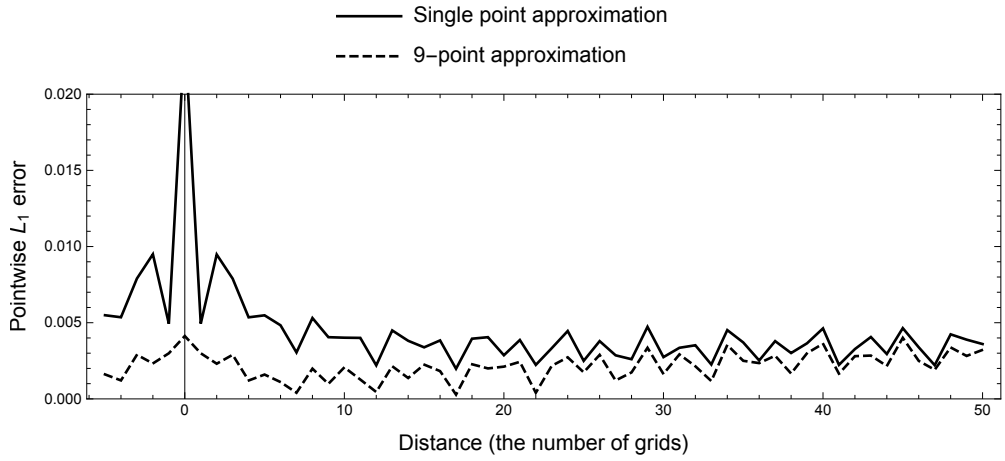

Figure 3.25: Pointwise L_1 error plot for $1/G = \tilde{k}h/2\pi = 0.40$. The solid line is computed from the single point approximation, and the dashed line is computed from the 9-point approximation of the impulse source.

3.2.2 3D 27-Point Method for a Homogeneous Medium

As in the 2D test, the numerical solutions were computed by the 27-point method for $\tilde{k}h/2\pi = 0.01$, 0.10, 0.20, 0.30 and 0.40. The size of the 3D computational domain was set to $(n_x \times n_y \times n_z) = (61 \times 61 \times 101)$ for $\tilde{k}h/2\pi = 0.10$, 0.20, 0.30 and 0.40. For $\tilde{k}h/2\pi = 0.01$, the size of the domain was increased to $(n_x \times n_y \times n_z) = (61 \times 61 \times 201)$ because relatively small imaginary part of the numerical solution (Figure 3.26) was affected by the slight reflection near the boundaries in spite of using the PML whose thickness is 20. The unit impulse source was discretized at the node $(i_x, i_y, i_z) = (31, 31, 31)$ for $\tilde{k}h/2\pi = 0.10$, 0.20, 0.30, 0.40 and at the node $(i_x, i_y, i_z) = (31, 31, 81)$ for $\tilde{k}h/2\pi = 0.01$, where $1 \le i_x \le n_x$, $1 \le i_y \le n_y$ and $1 \le i_z \le n_z$. For $\tilde{k}h/2\pi = 0.30$ and 0.40, the impulse source was approximated also by a set of discrete sources at the 27 neighbor nodes. The analytic solutions were computed by $\exp(ikr)/4\pi r$, and the value at the singular point $r = 0$ in the analytic solution was replaced by $\exp(ikh\epsilon)/4\pi h\epsilon$.

For each $\tilde{k}h$, we extracted a 1D line section parallel to z-direction, and the 1D line section contains the singularity of the 3D impulse response. From Figure 3.26 to Figure 3.32, we can see that the discrete and analytic solutions match well together. For $\tilde{k}h/2\pi = 0.30$ and 0.40, we can see that the numerical solutions from the 27-point impulse source approximation are better matched with the predicted value $\exp(ikh\epsilon)/4\pi h\epsilon$ at $r = 0$ than those of the single point approximation. Although Figure 3.33 and Figure 3.34 shows that the 27-point approximation of the impulse source has lower pointwise L_1 error than the single

point approximation, the single point approximation also reasonably matches the analytic solutions well as in 2D.

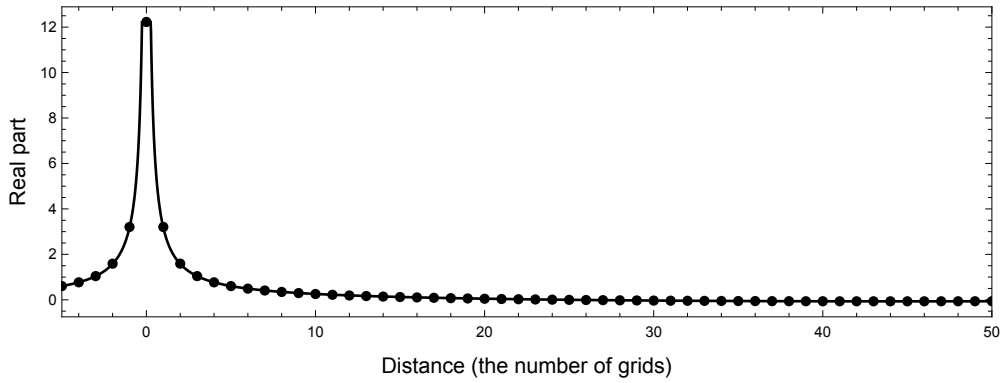

(a) Real part

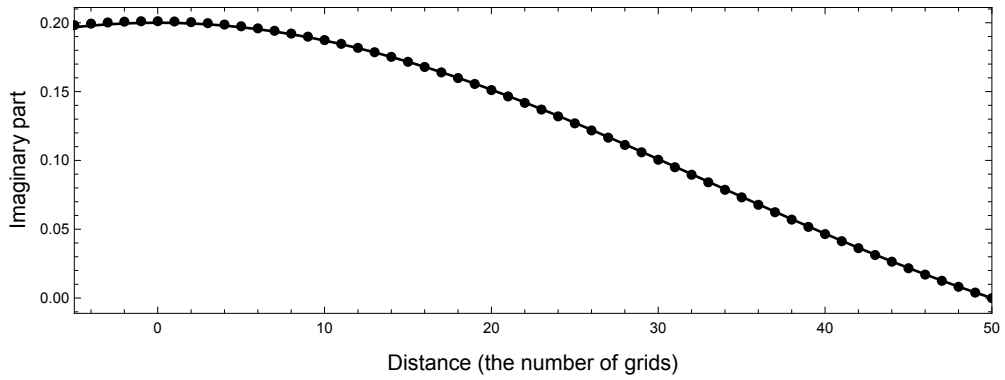

(b) Imaginary part

Figure 3.26: Comparison between the analytic solution (solid line) and the discrete solution (dots) when $1/G = \tilde{k}h/2\pi = 0.01$. The discrete solution is obtained from the proposed 27-point method of this thesis with the single point approximation of the impulse source.

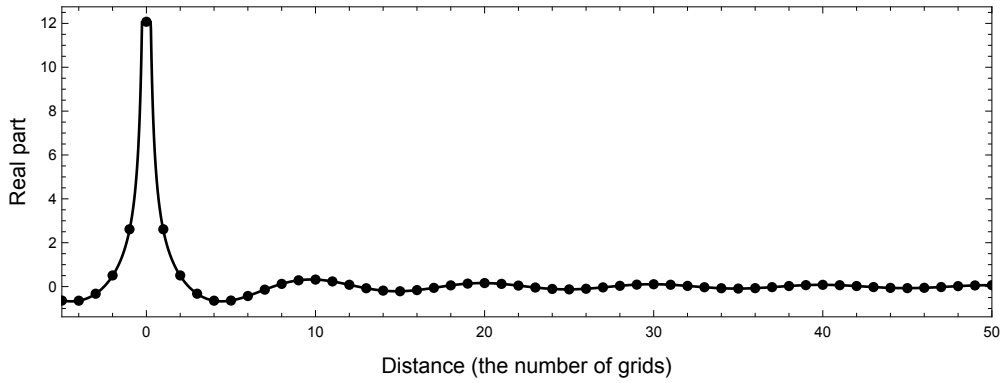

(a) Real part

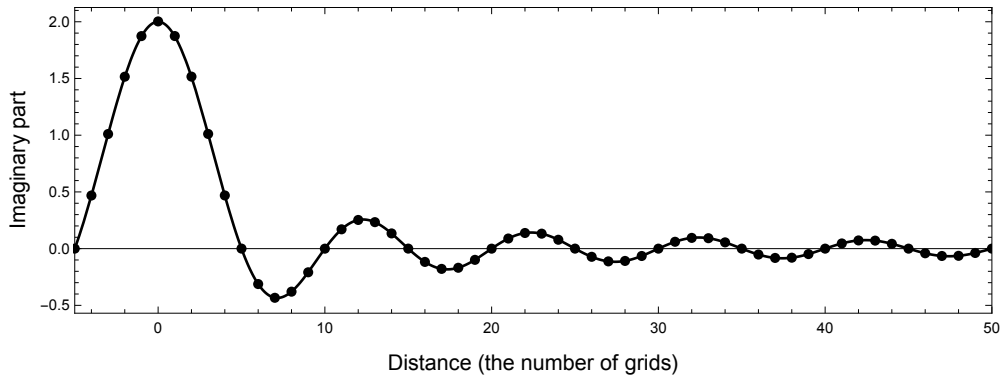

(b) Imaginary part

Figure 3.27: Comparison between the analytic solution (solid line) and the discrete solution (dots) when $1/G = \tilde{k}h/2\pi = 0.10$. The discrete solution is obtained from the proposed 27-point method of this thesis with the single point approximation of the impulse source.

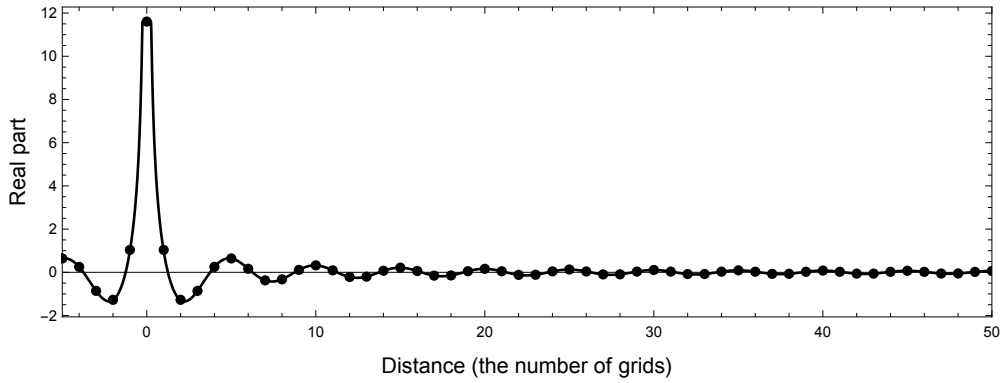

(a) Real part

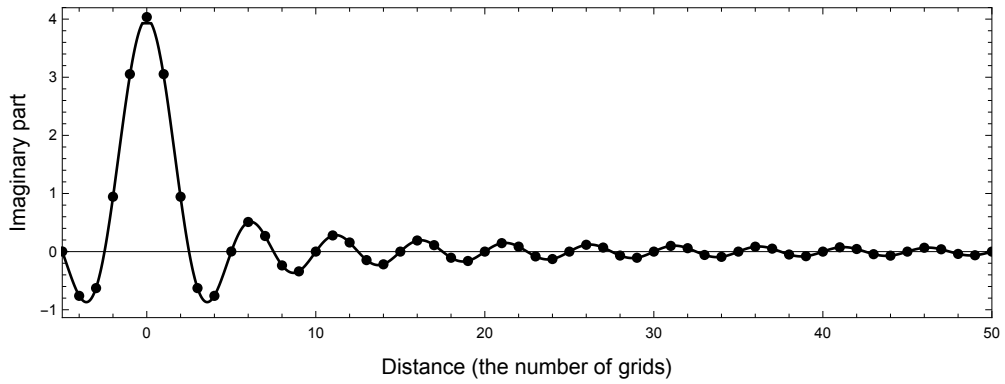

(b) Imaginary part

Figure 3.28: Comparison between the analytic solution (solid line) and the discrete solution (dots) when $1/G = \tilde{k}h/2\pi = 0.20$. The discrete solution is obtained from the proposed 27-point method of this thesis with the single point approximation of the impulse source.

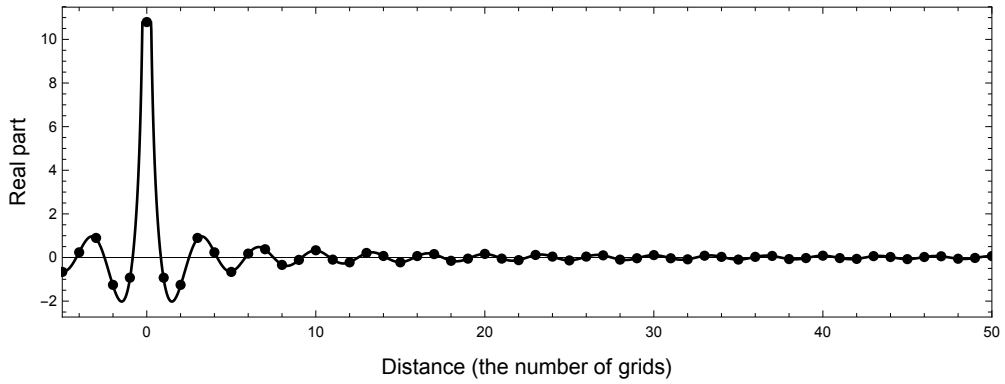

(a) Real part

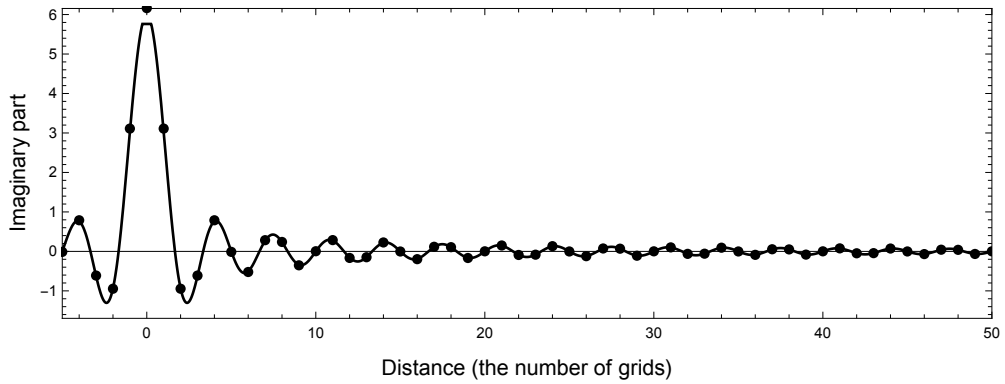

(b) Imaginary part

Figure 3.29: Comparison between the analytic solution (solid line) and the discrete solution (dots) when $1/G = \tilde{k}h/2\pi = 0.30$. The discrete solution is obtained from the proposed 27-point method of this thesis with the single point approximation of the impulse source.

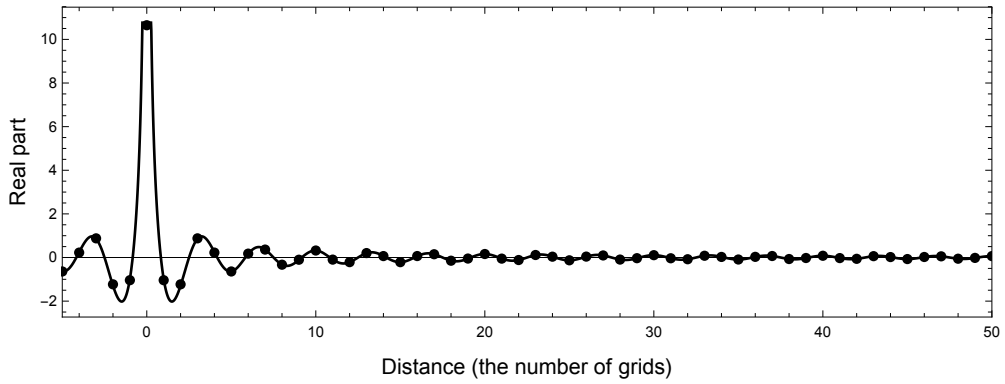

(a) Real part

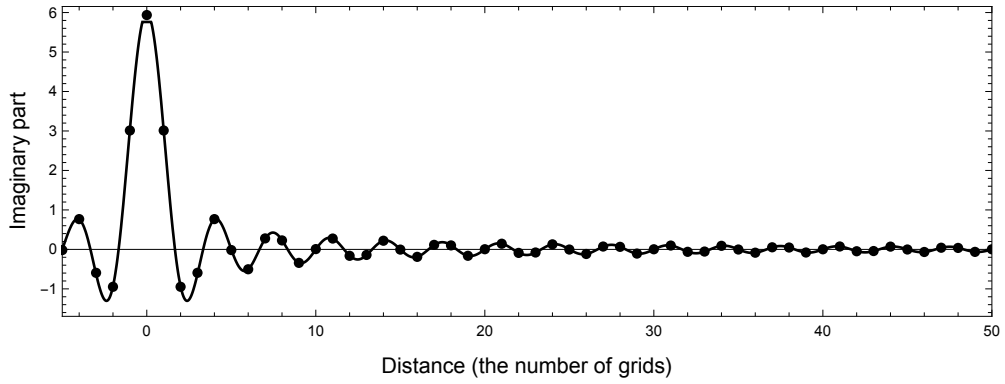

(b) Imaginary part

Figure 3.30: Comparison between the analytic solution (solid line) and the discrete solution (dots) when $1/G = \tilde{k}h/2\pi = 0.30$. The discrete solution is obtained from the proposed 27-point method of this thesis with the 27-point approximation of the impulse source.

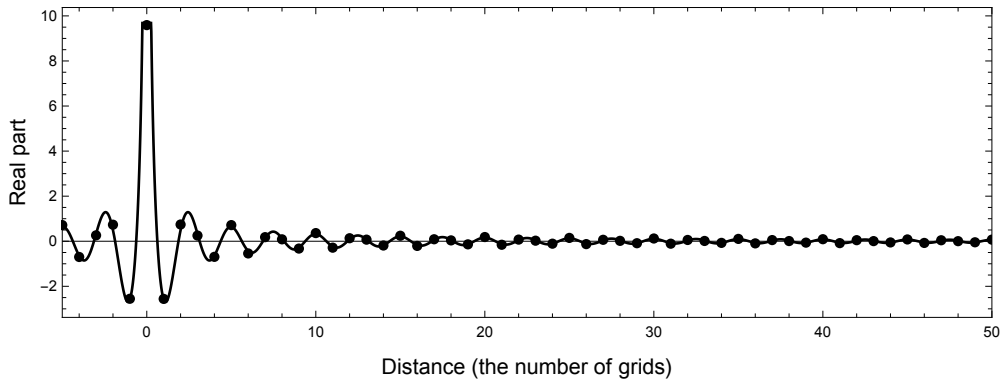

(a) Real part

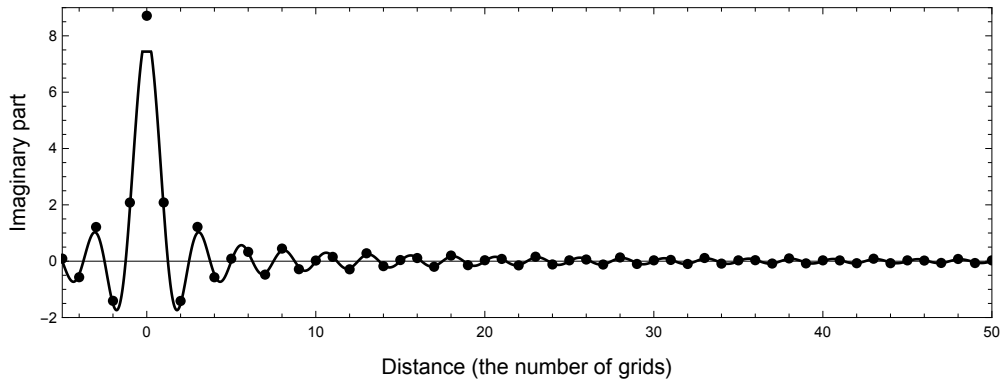

(b) Imaginary part

Figure 3.31: Comparison between the analytic solution (solid line) and the discrete solution (dots) when $1/G = \tilde{k}h/2\pi = 0.40$. The discrete solution is obtained from the proposed 27-point method of this thesis with the single point approximation of the impulse source.

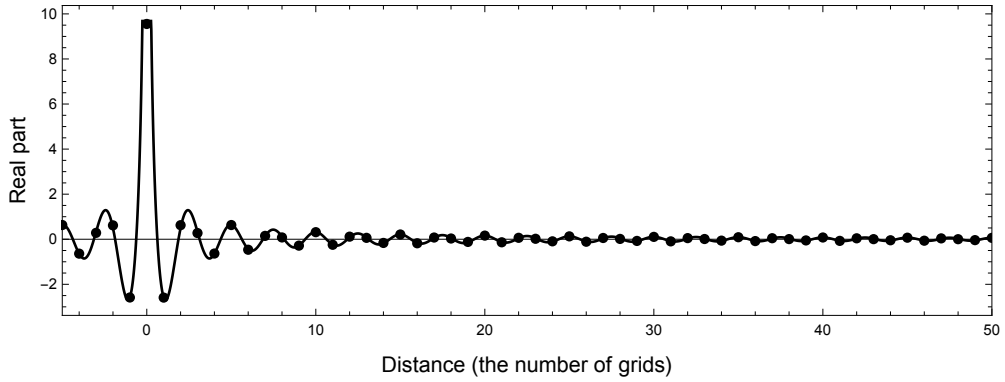

(a) Real part

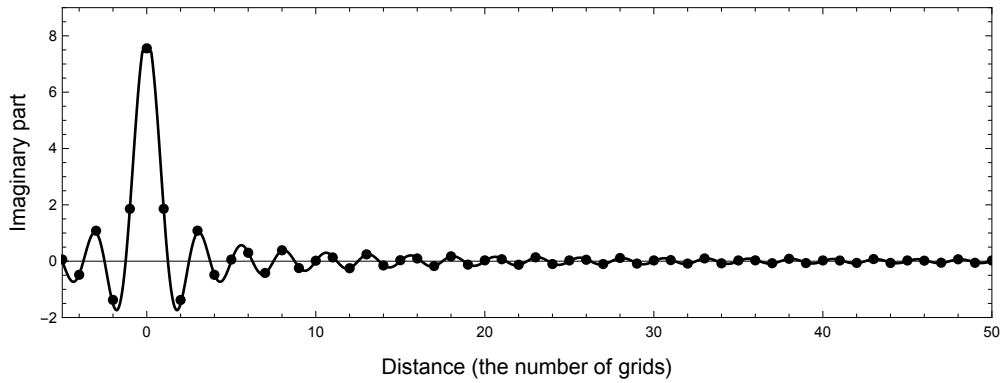

(b) Imaginary part

Figure 3.32: Comparison between the analytic solution (solid line) and the discrete solution (dots) when $1/G = \tilde{k}h/2\pi = 0.40$. The discrete solution is obtained from the proposed 27-point method of this thesis with the 27-point approximation of the impulse source.

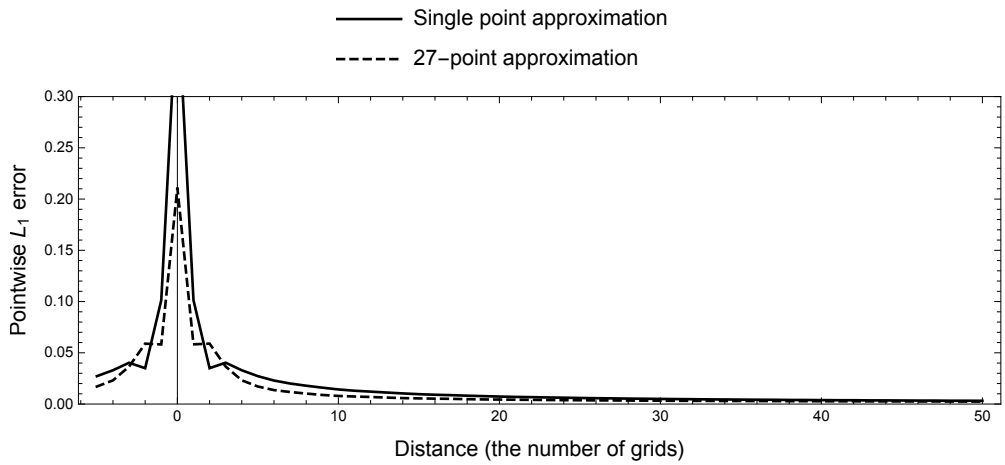

Figure 3.33: Pointwise L_1 error plot for $1/G = \tilde{k}h/2\pi = 0.30$. The solid line is computed from the single source approximation, and the dashed line is computed from the 27-point approximation.

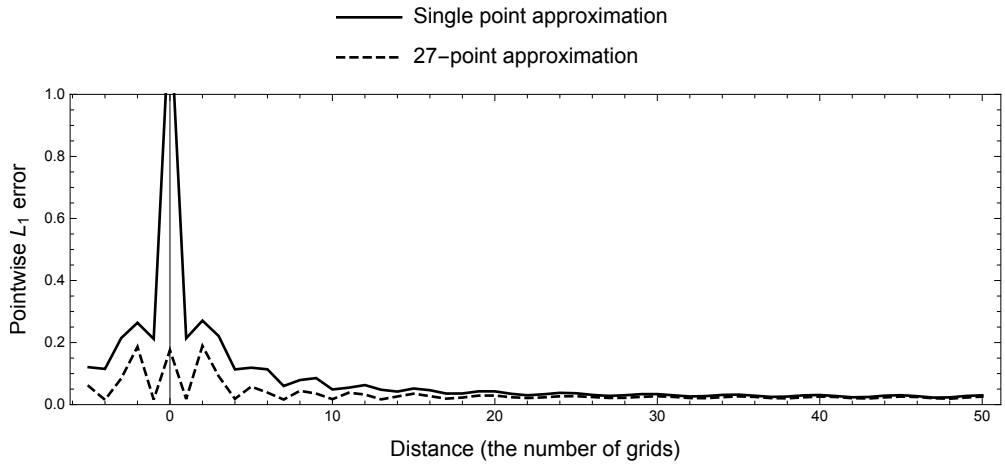

Figure 3.34: Pointwise L_1 error plot for $1/G = \tilde{k}h/2\pi = 0.40$. The solid line is computed from the single source approximation, and the dashed line is computed from the 27-point approximation.

3.2.3 2D Seismic Wave Propagation in Heterogeneous Media

From the previous numerical experiments for a homogeneous medium, the numerical solutions are matched well with the analytic solutions in the broad range of $\tilde{k}h$. However, the derivation of the proposed compact finite difference methods is based on the local homogeneity assumption, so the methods do not fully consider heterogeneity and there are first order errors at the interfaces (except for 1D, see Appendix A). Thus, the proposed methods would give inexact reflection and transmission coefficients if the grid interval h is not small enough. Nevertheless, the proposed methods can be used to simulate wave propagation in heterogeneous media to some extent. We compare the numerical solutions of our 2D 9-point compact finite difference method with the reference solutions obtained from the time domain modeling method of Tal-Ezer et al. (1987), which exactly considers heterogeneity without the numerical dispersion and the interface error due to exact time marching and spatial differentiations.

For comparison, we chose the Marmousi model (Versteeg, 1994), which is a classical heterogeneous acoustic wave speed model for seismic wave propagation. The velocity model is shown in Figure 3.35. The velocity increases as the depth deepens and the minimum and maximum velocity of the model is 1.5 km/s and 5.5 km/s, respectively. The velocity model was obtained by resampling and smoothing the original velocity model whose grid interval is 4 meters. The resampled grid interval h is 12.5 meters and the grid size is $(n_x \times n_z)=(736 \times 240)$, where x is Distance direction and z is Depth direction as shown in Figure 3.35. The time domain solution of our 9-point method was obtained by transform-

ing the frequency domain solution with the discrete Fourier transform. The reference time domain solution was obtained from time marching with Tal-Ezer et al. (1987)'s method. Most modeling conditions are the same for both modeling methods: The maximum recording time $T_{\max}$ is 4 seconds. Also, the maximum frequency $f_{\max}$ is about 30 Hz and the time interval Δt is $1/(2f_{\max})$. We can compute the number of grids per minimum wavelength $G = 4$ using the minimum velocity 1.5 km/s, the maximum frequency $f_{\max} = 30$ Hz and the grid interval $h = 12.5$ m. The boundary conditions of our 9-point method is the frequency domain PML (see Appendix B), and the boundary condition of Tal-Ezer et al. (1987)'s method is a variant of the time domain PML (Park et al., 2014). The PML was set in the four boundaries and the thickness (the number of grids) of the PML is 20. The source wavelet is a shifted Ricker wavelet defined as

$$w(t) = (1 - 2\pi^2(f_{\text{peak}}t - 1.1)^2)\exp(-\pi^2(f_{\text{peak}}t - 1.1))^2), \tag{3.20}$$

where $f_{\text{peak}} \approx f_{\max}/3 = 10$ Hz is the peak frequency whose amplitude is the maximum in the frequency spectrum. In the 9-point method, the spatial impulse source with the Ricker wavelet was set at the center of the computational domain. In Tal-Ezer et al. (1987)'s method, the spatial distribution of the impulse source was approximated by a narrow Gaussian bell shaped distribution. For both cases, the receiver line was set parallel to x (Distance) direction through the center of the domain

As shown in Figure 3.36, both seismograms from the receiver line are virtually indistinguishable with the naked eye. Time traces at some distances are also shown in Figure 3.37 and the traces are matched well.

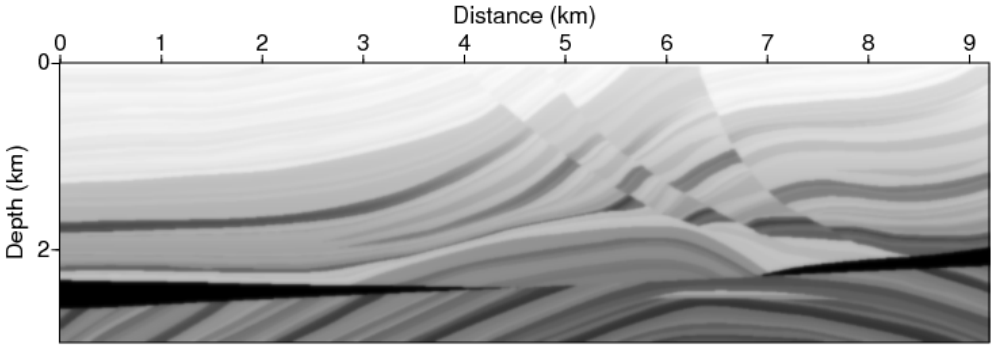

Figure 3.35: The Marmousi P-wave velocity model

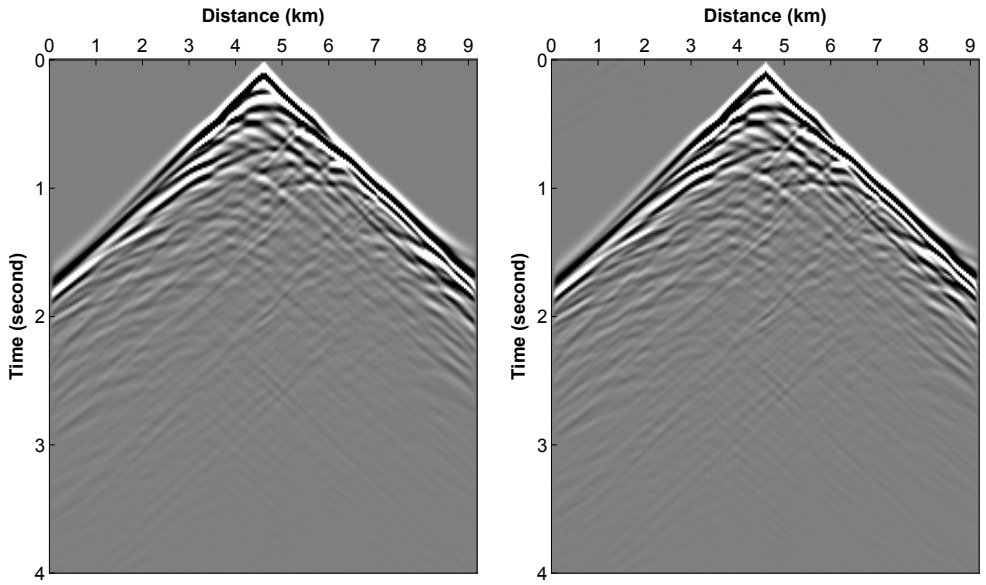

(a) Tal-Ezer's method

(b) 9-point method

Figure 3.36: Time domain seismograms from Tal-Ezer and the 9-point method

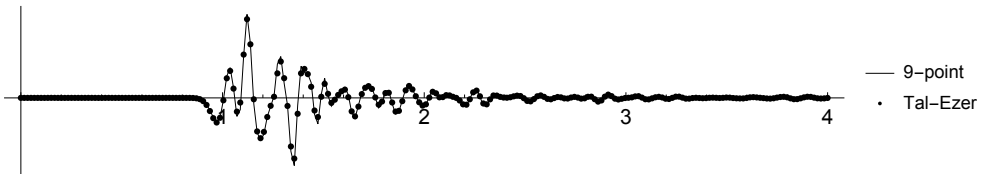

(a) Traces at 2 km distance

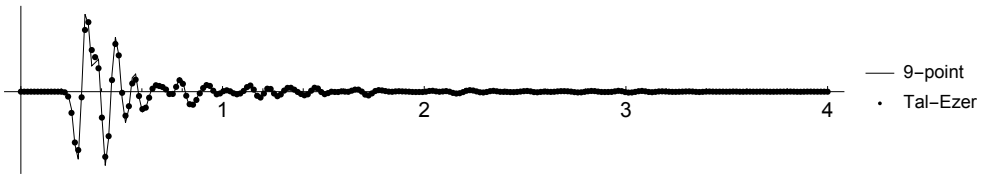

(b) Traces at 4 km distance

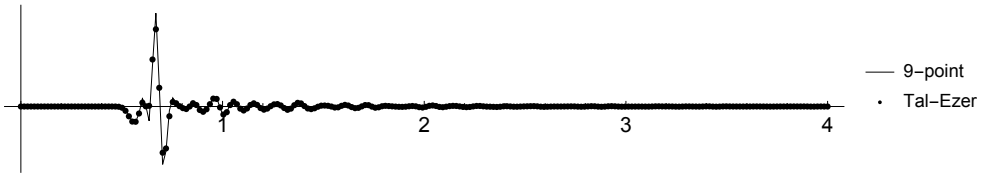

(c) Traces at 6 km distance

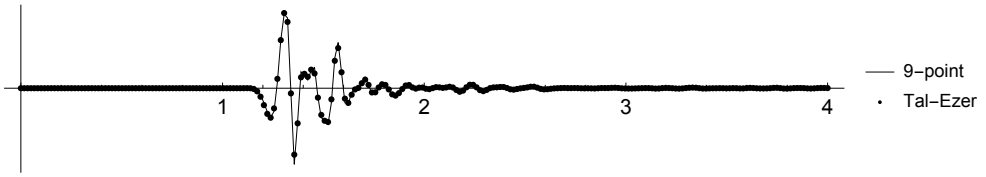

(d) Traces at 8 km distance

Figure 3.37: Comparison of time domain traces between Tal-Ezer's method and the 9-point method

Chapter 4

Conclusions

The compact finite difference methods using the analytic basis functions were introduced, and we verified the high accuracy of the proposed methods in terms of the dispersion error and the amplitude of the impulse response in the wide range of $\tilde{k}h$. Although the proposed methods are based on the homogeneity assumption, the numerical experiements showed that the methods can simulate reasonably well seismic wave propagation in hetereogeneous media. Thus, large scale geophysical applications with the impulse sources on Cartesian grids such as full waveform inversion (Tarantola, 1984; Shin, 1988; Pratt et al., 1998; Virieux and Operto, 2009) in the exploration geophysics would benefit from the accuracy and efficiency of the proposed methods.

Appendix A

Exact 1D Discretization with Piecewise-Constant Media

A.1 Derivation

We consider the 1D Helmholtz equation

$$-\frac{k^2}{\rho}u - \frac{\partial}{\partial x}\frac{1}{\rho}\frac{\partial u}{\partial x} = f \tag{A.1}$$

with the piecewise-constant wavenumber k and density ρ. The 1D shifting operator (Equation (2.21)) can be used to derive a finite difference expression for the piecewise-constant material distribution. In Figure A.1, the first derivatives are discontinuous due to the discontinuous media at $x = 0$. We can analytically write neighbor nodal points as

$$u_1 := u(h) = \cos(k_{\frac{1}{2}}h)u_0^+ + \operatorname{sinc}(k_{\frac{1}{2}}h)h\partial_x u_0^+, \tag{A.2}$$

$$u_{-1} := u(-h) = \cos(k_{-\frac{1}{2}}h)u_0^- - \operatorname{sinc}(k_{-\frac{1}{2}}h)h\partial_x u_0^-. \tag{A.3}$$

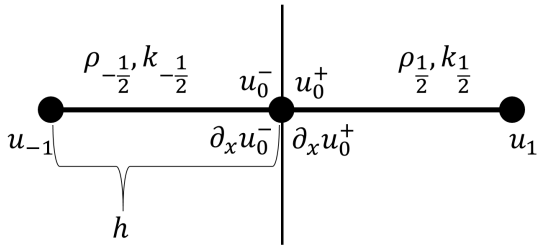

Figure A.1: 1D stencil for piecewise-constant heterogeneous media

There are two conditions should be met as follows

$$u_0^- = u_0^+, \tag{A.4}$$

$$\frac{1}{\rho_{-\frac{1}{2}}}\frac{\partial u_0^-}{\partial x} = \frac{1}{\rho_{\frac{1}{2}}}\frac{\partial u_0^+}{\partial x}. \tag{A.5}$$

The first one (Equation (A.4)) is the pressure continuity condition and the second one (Equation (A.5)) is the normal velocity continuity condition. Using these two conditions, the first derivatives can be cancelled out to form the following three term expression

$$\frac{u_{-1}}{\rho_{-\frac{1}{2}}\mathrm{sinc}(k_{-\frac{1}{2}}h)} + \frac{u_1}{\rho_{\frac{1}{2}}\mathrm{sinc}(k_{\frac{1}{2}}h)} = \left(\frac{\cos(k_{-\frac{1}{2}}h)}{\rho_{-\frac{1}{2}}\mathrm{sinc}(k_{-\frac{1}{2}}h)} + \frac{\cos(k_{\frac{1}{2}}h)}{\rho_{\frac{1}{2}}\mathrm{sinc}(k_{\frac{1}{2}}h)}\right)u_0, \tag{A.6}$$

where $u_0 = u_0^- = u_0^+$.

If there is an impulse source $f(x) = \alpha_0\delta(x - x_0)$, which is located at $x = x_0$, then a jump of the normal velocity occurs as follows

$$\frac{1}{\rho_{-\frac{1}{2}}}\frac{\partial u_0^-}{\partial x} + \alpha_0 = \frac{1}{\rho_{\frac{1}{2}}}\frac{\partial u_0^+}{\partial x}, \tag{A.7}$$

which gives

$$\frac{u_{-1}}{\rho_{-\frac{1}{2}}\mathrm{sinc}(k_{-\frac{1}{2}}h)} + \frac{u_1}{\rho_{\frac{1}{2}}\mathrm{sinc}(k_{\frac{1}{2}}h)} = \left(\frac{\cos(k_{-\frac{1}{2}}h)}{\rho_{-\frac{1}{2}}\mathrm{sinc}(k_{-\frac{1}{2}}h)} + \frac{\cos(k_{\frac{1}{2}}h)}{\rho_{\frac{1}{2}}\mathrm{sinc}(k_{\frac{1}{2}}h)}\right)u_0 + \alpha_0 h. \tag{A.8}$$

Using the finite difference operator δ_x, Equation (A.8) can be rewritten as

$$-\frac{1}{h^2}\left(\frac{1-\cos(k_{-\frac{1}{2}}h)}{\rho_{-\frac{1}{2}}\,\mathrm{sinc}(k_{-\frac{1}{2}}h)}+\frac{1-\cos(k_{\frac{1}{2}}h)}{\rho_{\frac{1}{2}}\,\mathrm{sinc}(k_{\frac{1}{2}}h)}\right)u_0-\delta_x\frac{1}{\rho\,\mathrm{sinc}(kh)}\delta_x u_0=\frac{\alpha_0}{h}, \quad \text{(A.9)}$$

which does not produce any discretization error. Of course, discretization error may be introduced when the actual discontinuous interface is not exactly matched with the grid interface, or when the continuous problem has smooth profiles of the density ρ and the wavenumber k.

If we assume homogeneous medium ($\rho_{-\frac{1}{2}}=\rho_{\frac{1}{2}}=\rho$ and $k_{-\frac{1}{2}}=k_{\frac{1}{2}}=k$), then Equation (A.9) reduces to

$$-\frac{1}{h^2}\left(\frac{2-2\cos(kh)}{\rho\,\mathrm{sinc}(kh)}\right)u_0-\delta_x\frac{1}{\rho\,\mathrm{sinc}(kh)}\delta_x u_0=\frac{\alpha_0}{h}, \quad \text{(A.10)}$$

which is similar to Equation (2.76) in Section 2.5.1. The only difference between the two equations is the location of the $\mathrm{sinc}(kh)$ function. In Equation (A.9) and Equation (A.10), the $\mathrm{sinc}(kh)$ function can be thought of as a correction term to compute an effective density $\tilde{\rho}=\rho\,\mathrm{sinc}(kh)$. We rewrite Equation (A.9) with the effective density $\tilde{\rho}$ as follows

$$-\frac{1}{h^2}\left(\frac{1-\cos(k_{-\frac{1}{2}}h)}{\tilde{\rho}_{-\frac{1}{2}}}+\frac{1-\cos(k_{\frac{1}{2}}h)}{\tilde{\rho}_{\frac{1}{2}}}\right)u_0-\delta_x\frac{1}{\tilde{\rho}}\delta_x u_0=\frac{\alpha_0}{h}, \quad \text{(A.11)}$$

where the finite volume approximation α_0/h of the Dirac delta function can be used as a source term without correction, because $\mathrm{sinc}(kh)$ is absorbed to the effective density $\tilde{\rho}$.

Appendix B

Perfectly Matched Layer

B.1 Continuous Perfectly Matched Layer

The Perfectly Matched Layer (Bérenger, 1994, 2007) has the ability to suppress spurious reflections at the boundaries of the computational domain. In the frequency domain, the PML can be easily introduced by using the following complex coordinate stretching (Chew and Weedon, 1994)

$$\begin{aligned} \partial_x &\to \frac{1}{s_x}\partial_x, \\ \partial_y &\to \frac{1}{s_y}\partial_y, \\ \partial_z &\to \frac{1}{s_z}\partial_z, \end{aligned} \tag{B.1}$$

where s_x and s_z are the complex coordinate stretching parameters. If we apply the complex coordinate stretching to the 2D Helmholtz equation, then we obtain

the Helmholtz equation with the PML coefficients as follows

$$-k^2u - \frac{1}{s_x}\frac{\partial}{\partial x}\frac{1}{s_x}\frac{\partial u}{\partial x} - \frac{1}{s_y}\frac{\partial}{\partial y}\frac{1}{s_y}\frac{\partial u}{\partial y} = 0. \tag{B.2}$$

Multiplying $s_x s_y$ to Equation (B.2) gives

$$-k^2 s_x s_y u - \frac{\partial}{\partial x}\frac{s_y}{s_x}\frac{\partial u}{\partial x} - \frac{\partial}{\partial y}\frac{s_x}{s_y}\frac{\partial u}{\partial y} = 0. \tag{B.3}$$

Either Equation (B.2) or Equation (B.3) can be used, but Equation (B.3) may be more preferred, because Equation (B.3) can be discretized by using a symmetric indefinite matix. If a direct sparse matrix solver such as a multifrontal solver is used, then the symmetric indefinite matrix can be factorized by the LDLT (LDL^T) decomposition with the Bunch-Kaufman 2×2 diagonal pivoting (Bunch and Kaufman, 1977). The LDLT decomposition can reduce the arithmetic operations and the memory requirement roughly by half, compared to the LU decomposition.

We can also apply the complex coordinate stretching to the 3D Helmholtz equation as follows

$$-k^2u - \frac{1}{s_x}\frac{\partial}{\partial x}\frac{1}{s_x}\frac{\partial u}{\partial x} - \frac{1}{s_y}\frac{\partial}{\partial y}\frac{1}{s_y}\frac{\partial u}{\partial y} - \frac{1}{s_y}\frac{\partial}{\partial y}\frac{1}{s_y}\frac{\partial u}{\partial y} = 0. \tag{B.4}$$

Multiplying $s_x s_y s_z$ to Equation (B.4) gives

$$-k^2 s_x s_y s_z u - \frac{\partial}{\partial x}\frac{s_y s_z}{s_x}\frac{\partial u}{\partial x} - \frac{\partial}{\partial y}\frac{s_z s_x}{s_y}\frac{\partial u}{\partial y} - \frac{\partial}{\partial z}\frac{s_x s_y}{s_z}\frac{\partial u}{\partial z} = 0. \tag{B.5}$$

B.2 Discrete Perfectly Matched Layer in 1D

In 1D problem, the complex coordinate stretching gives

$$-k^2u - \frac{1}{s_x}\frac{\partial}{\partial x}\frac{1}{s_x}\frac{\partial u}{\partial x} = 0. \tag{B.6}$$

If we assume piecewise constant media, the wavenumber k and the PML parameter s_x is constant within one grid cell. Then Equation (B.6) becomes

$$-k^2 u - \frac{1}{s_x^2}\frac{\partial^2 u}{\partial x^2} = 0, \tag{B.7}$$

and subsequently,

$$-k^2 s_x^2 u - \frac{\partial^2 u}{\partial x^2} = 0. \tag{B.8}$$

So, the PML coefficient s_x can be absorbed to the wavenumber k. Then, we can just use the equation for the piecsewise constant heterogeneous media (Equation (A.8) or Equation (A.9)) with the modified wavenumber $k \to k s_x$. This discretization method of the 1D PML does not introduce any discretization error.

B.3 Discrete Perfectly Matched Layer in 2D and 3D

In contrast to the 1D problem, the exact discretization of the PML cannot be achieved in the 2D and 3D problems. We may try the following complex coordinate stretching in the discrete level, which is analogous to the continuous version of the complex coordinate stretcing (Equation (B.1)).

$$\begin{aligned} \delta_x &\to \frac{1}{s_x}\delta_x, \\ \delta_y &\to \frac{1}{s_y}\delta_y, \\ \delta_z &\to \frac{1}{s_z}\delta_z. \end{aligned} \tag{B.9}$$

If we apply the discrete complex coordinate stretching to the 2D 9-point method (Equation (2.50)), then, we obtain the following equation

$$-\frac{L_9(kh)}{h^2}u_{0,0}-\left(\frac{1}{s_x}\delta_x\frac{1}{s_x}\delta_x+\frac{1}{s_y}\delta_y\frac{1}{s_y}\delta_y\right)u_{0,0}-h^2\frac{1}{s_x}\delta_x\frac{1}{s_y}\delta_y M_9(kh)\frac{1}{s_x}\delta_x\frac{1}{s_y}\delta_y u_{0,0}=0. \tag{B.10}$$

Multiplying $s_x s_y$ to Equation (B.10), we can obtain the symmetric discretization of the Helmholtz equation with the PML as follows

$$-\frac{L_9(kh)}{h^2}s_x s_y u_{0,0}-\left(\delta_x\frac{s_y}{s_x}\delta_x+\delta_y\frac{s_x}{s_y}\delta_y\right)u_{0,0}-h^2\delta_x\delta_y\frac{M_9(kh)}{s_x s_y}\delta_x\delta_y u_{0,0}=0. \tag{B.11}$$

If we have the variable density ρ, then Equation (B.11) can be approximately modified to

$$-\frac{L_9(kh)}{h^2}\frac{s_x s_y}{\rho}u_{0,0}-\left(\delta_x\frac{s_y}{\rho s_x}\delta_x+\delta_y\frac{s_x}{\rho s_y}\delta_y\right)u_{0,0}-h^2\delta_x\delta_y\frac{M_9(kh)}{\rho s_x s_y}\delta_x\delta_y u_{0,0}=0, \tag{B.12}$$

which reduces to Equation (B.11) when ρ is constant.

We can apply the discrete complex coordinate stretching to the 3D discrete Helmholtz equation (Equation (2.69)) as follows

$$\begin{aligned}-\frac{L_{27}(kh)}{h^2}u_{0,0,0}-\left(\frac{1}{s_x}\delta_x\frac{1}{s_x}\delta_x+\frac{1}{s_y}\delta_y\frac{1}{s_y}\delta_y+\frac{1}{s_z}\delta_z\frac{1}{s_z}\delta_z\right)u_{0,0,0}\\ -h^2\frac{1}{s_x}\delta_x\frac{1}{s_y}\delta_y M_{27}(kh)\frac{1}{s_x}\delta_x\frac{1}{s_y}\delta_y u_{0,0,0}\\ -h^2\frac{1}{s_y}\delta_y\frac{1}{s_z}\delta_z M_{27}(kh)\frac{1}{s_y}\delta_y\frac{1}{s_z}\delta_z u_{0,0,0}\\ -h^2\frac{1}{s_z}\delta_z\frac{1}{s_x}\delta_x M_{27}(kh)\frac{1}{s_z}\delta_z\frac{1}{s_x}\delta_x u_{0,0,0}\\ -h^4\frac{1}{s_x}\delta_x\frac{1}{s_y}\delta_y\frac{1}{s_z}\delta_z N_{27}(kh)\frac{1}{s_x}\delta_x\frac{1}{s_y}\delta_y\frac{1}{s_z}\delta_z u_{0,0,0}=0.\end{aligned} \tag{B.13}$$

Multiplying $s_x s_y s_z$ to Equation (B.14) gives

$$\begin{aligned}
-\frac{L_{27}(kh)}{h^2} s_x s_y s_z u_{0,0,0} - \left(\delta_x \frac{s_y s_z}{s_x} \delta_x + \delta_y \frac{s_z s_x}{s_y} \delta_y + \delta_z \frac{s_x s_y}{s_z} \delta_z \right) u_{0,0,0} \\
-h^2 \delta_x \delta_y \frac{M_{27}(kh) s_z}{s_x s_y} \delta_x \delta_y u_{0,0,0} \\
-h^2 \delta_y \delta_z \frac{M_{27}(kh) s_x}{s_y s_z} \delta_y \delta_z u_{0,0,0} \\
-h^2 \delta_z \delta_x \frac{M_{27}(kh) s_y}{s_z s_x} \delta_z \delta_x u_{0,0,0} \\
-h^4 \delta_x \delta_y \delta_z \frac{N_{27}(kh)}{s_x s_y s_z} \delta_x \delta_y \delta_z u_{0,0,0} = 0,
\end{aligned} \tag{B.14}$$

which is a symmetric discretization of the 3D Helmholtz equation with the PML. We can also approximately include the density ρ into Equation (B.14) as follows

$$\begin{aligned}
-\frac{L_{27}(kh)}{h^2} \frac{s_x s_y s_z}{\rho} u_{0,0,0} - \left(\delta_x \frac{s_y s_z}{\rho s_x} \delta_x + \delta_y \frac{s_z s_x}{\rho s_y} \delta_y + \delta_z \frac{s_x s_y}{\rho s_z} \delta_z \right) u_{0,0,0} \\
-h^2 \delta_x \delta_y \frac{M_{27}(kh) s_z}{\rho s_x s_y} \delta_x \delta_y u_{0,0,0} \\
-h^2 \delta_y \delta_z \frac{M_{27}(kh) s_x}{\rho s_y s_z} \delta_y \delta_z u_{0,0,0} \\
-h^2 \delta_z \delta_x \frac{M_{27}(kh) s_y}{\rho s_z s_x} \delta_z \delta_x u_{0,0,0} \\
-h^4 \delta_x \delta_y \delta_z \frac{N_{27}(kh)}{\rho s_x s_y s_z} \delta_x \delta_y \delta_z u_{0,0,0} = 0.
\end{aligned} \tag{B.15}$$

Bibliography

L. Banjai and W. Hackbusch. Hierarchical matrix techniques for low-and high-frequency Helmholtz problems. *IMA journal of numerical analysis*, 2007.

J.-P. Bérenger. A perfectly matched layer for the absorption of electromagnetic waves. *Journal of computational physics*, 114(2):185–200, 1994.

J.-P. Bérenger. Perfectly matched layer (PML) for computational electromagnetics. *Synthesis Lectures on Computational Electromagnetics*, 2(1):1–117, 2007.

J. R. Bunch and L. Kaufman. Some stable methods for calculating inertia and solving symmetric linear systems. *Mathematics of computation*, pages 163–179, 1977.

W. C. Chew and W. H. Weedon. A 3d perfectly matched medium from modified Maxwell's equations with stretched coordinates. *Microwave and optical technology letters*, 7(13):599–604, 1994.

C. W. Clenshaw. A note on the summation of Chebyshev series. *Mathematics of Computation*, 9(51):118–120, 1955.

M. J. Gander and H. Zhang. Iterative solvers for the Helmholtz equation: Factorizations, sweeping preconditioners, source transfer, single layer potentials, polarized traces, and optimized Schwarz methods. *arXiv preprint arXiv:1610.02270*, 2016.

R. Hiptmair, A. Moiola, and I. Perugia. A survey of Trefftz methods for the Helmholtz equation. In *Building Bridges: Connections and Challenges in Modern Approaches to Numerical Partial Differential Equations*, pages 237–278. Springer, 2016.

W. G. Horner. A new method of solving numerical equations of all orders, by continuous approximation. *Philosophical Transactions of the Royal Society of London*, 109:308–335, 1819.

C.-H. Jo, C. Shin, and J. H. Suh. An optimal 9-point, finite-difference, frequency-space, 2-d scalar wave extrapolator. *Geophysics*, 61(2):529–537, 1996.

J. Lee. *Arbitrary-order symplectic time integrator for the acoustic wave equation using the pseudo-spectral method.* PhD thesis, Seoul National University, 2017.

K. J. Marfurt. Accuracy of finite-difference and finite-element modeling of the scalar and elastic wave equations. *Geophysics*, 49(5):533–549, 1984.

M. Nabavi, M. K. Siddiqui, and J. Dargahi. A new 9-point sixth-order accurate compact finite-difference method for the Helmholtz equation. *Journal of Sound and Vibration*, 307(3):972–982, 2007.

J. W. Nehrbass, J. O. Jevtic, and R. Lee. Reducing the phase error for finite-difference methods without increasing the order. *IEEE Transactions on Antennas and Propagation*, 46(8):1194–1201, 1998.

S. Operto, J. Virieux, P. Amestoy, J.-Y. L'Excellent, L. Giraud, and H. B. H. Ali. 3d finite-difference frequency-domain modeling of visco-acoustic wave propagation using a massively parallel direct solver: A feasibility study. *Geophysics*, 72(5):SM195–SM211, 2007.

H. Park, J. Lee, K. Lee, and C. Shin. A split formulation of the nearly perfectly matched layer for an acoustic wave equation using the discontinuous Galerkin method. In *SEG Technical Program Expanded Abstracts 2014*, pages 3344–3348. Society of Exploration Geophysicists, 2014.

R. G. Pratt, C. Shin, and G. Hick. Gauss–Newton and full Newton methods in frequency–space seismic waveform inversion. *Geophysical Journal International*, 133(2):341–362, 1998.

C. Shin. *Nonlinear elastic wave inversion by blocky parameterization.* PhD thesis, University of Tulsa, 1988.

I. Singer and E. Turkel. High-order finite difference methods for the Helmholtz equation. *Computer Methods in Applied Mechanics and Engineering*, 163 (1-4):343–358, 1998.

I. Singer and E. Turkel. Sixth-order accurate finite difference schemes for the Helmholtz equation. *Journal of Computational Acoustics*, 14(03):339–351, 2006.

G. Sutmann. Compact finite difference schemes of sixth order for the Helmholtz equation. *Journal of Computational and Applied Mathematics*, 203(1):15–31, 2007.

H. Tal-Ezer, D. Kosloff, and Z. Koren. An accurate scheme for seismic forward modelling. *Geophysical Prospecting*, 35(5):479–490, 1987.

A. Tarantola. Inversion of seismic reflection data in the acoustic approximation. *Geophysics*, 1984.

I. Tsukerman. A class of difference schemes with flexible local approximation. *Journal of Computational Physics*, 211(2):659–699, 2006.

R. Versteeg. The Marmousi experience: Velocity model determination on a synthetic complex data set. *The Leading Edge*, 13(9):927–936, 1994. ISSN 1070-485X. doi: 10.1190/1.1437051.

J. Virieux and S. Operto. An overview of full-waveform inversion in exploration geophysics. *Geophysics*, 2009.

S. Wang, M. V. de Hoop, and J. Xia. On 3d modeling of seismic wave propagation via a structured parallel multifrontal direct Helmholtz solver. *Geophysical Prospecting*, 59(5):857–873, 2011.

초록

본 논문에서는 헬름홀츠 방정식의 해석적 기저함수를 이용한 컴팩트 유한차분법을 유도한다. 해석적인 정보를 활용하는 본 방법은 수치적인 분산 오차를 크게 줄임으로써, 기존의 컴팩트 유한차분법에 비해 수치 시뮬레이션에 사용되는 파장 당 최소 격자 수를 낮출 수 있다. 이를 통해, 사용되는 격자 수를 늘리지 않고서도 높은 주파수 혹은 파수 영역에 대한 시뮬레이션을 가능하게 해주므로 계산량이 감소한다. 효율성과 정확성이 높은 본 컴팩트 유한차분법은 정규 격자를 이용한 계산량이 큰 응용 분야에 매우 적합하다. 제안된 방법의 효율성과 정확성을 확인하기 위해 수치적인 결과를 보이고 이를 비교한다. 또한, 비균질 매질에서의 지진파 전파에 본 방법을 적용해보고 본 방법의 지구물리 응용 분야에 대한 적용성을 가늠한다.

주요어: 헬름홀츠 방정식, 트레프츠 기저 함수, 유한 차분, 수치적 분산 오차, 지진파

학번: 2010-23217